Coppola, L., Reder, A., Rianna, G., Tarantino, A., & Pagano, L. (in press). Effects of Wooden Embers Cover on thermo-hydrological response of silty volcanic cover and implications to post-wildfire slope stability. *Engineering Geology*.

Effects of Wooden Embers Cover on thermo-hydrological response of silty volcanic cover and implications to post-wildfire slope stability

Coppola L. [1], Reder A.[2], Rianna G.[2], Tarantino A. [3], Pagano L.[1]

[1] Dipartimento di Ingegneria civile, edile e ambientale, Università di Napoli Federico II, Italy

[2] CMCC Foundation - Euro-Mediterranean Center on Climate Change, Italy

[3] Department of Civil and Environmental Engineering, University of Strathclyde, Scotland, UK

CORRESPONDING AUTHOR: lucia.coppola@unina.it

Abstract

Wildfires striking vegetated hillslopes appear to increase the hazard towards rainfall-induced landslides. One mechanism little investigated in the literature consists in the formation of Wooden Embers Cover (WEC) following the wildfire. This layer has very peculiar thermohydraulic properties and may affect the interaction between the atmosphere and the subsoil. The paper presents an experiment conducted in an outdoor lysimeter filled with pyroclastic silt (SILT) up to 75 cm covered with 5 cm of WEC. Water storage in the SILT layer, soil water content, suction, and temperature were recorded for several years, initially under bare (no-WEC) condition (4 years), then vegetated (no-WEC) condition (5 years) and, finally, with a WEC placed on the top of the SILT (SILT+WEC condition; 3 years). The hydrological effect of the WEC was assessed by comparing the response of the SILT+WEC with the SILT under bare or vegetated conditions. The WEC reduces water losses by evaporation, thus increasing the average water content in the underlying SILT, an effect that is detrimental to slope stability. To discriminate whether the barrier effect was associated with the lower thermal or hydraulic conductivity of the WEC, a numerical simulation was carried out by considering the case of a WEC with its real thermal and hydraulic properties and the case of a fictitious top layer placed on the top of the SILT having the same hydraulic properties of the WEC but the thermal properties of the SILT. It is concluded that the barrier effect of the WEC is mainly associated with its hydraulic properties, i.e. the WEC acts as a capillary barrier. To demonstrate the practical implications of this findings, a case study of rainfall-induced landslide has been reanalysed by simulating the presence of a WEC layer having the same thermohydraulic properties as the material characterised in this study. It is shown that a WEC can substantially reduce the severity of the triggering rainfall event, thus increasing the vulnerability of the slope to rainfall-induced failure.

Coppola, L., Reder, A., Rianna, G., Tarantino, A., & Pagano, L. (in press). Effects of Wooden Embers Cover on thermo-hydrological response of silty volcanic cover and implications to post-wildfire slope stability. *Engineering Geology*.

1. Introduction

Wildfires striking vegetated hillslopes appear to increase the hazard towards rainfall-induced landslides (Rengers et al., 2020; Ferreira et al., 2009; Silva et al., 2010, Bernard et al., 2020, Abdollahi et al., 2024). The burning of vegetation has been observed to reduce the return period of rainfalls triggering shallow landslides at the catchment scale in Italy (Esposito et al., 2023), USA (Kean et al., 2011; Staley et al., 2013, 2020; Kampf et al., 2016; Raymond et al., 2020), Greece (Filis et al., 2020; Lainas et al., 2021), Spain (Mayor et al., 2007), and Portugal (Lourenco et al., 2012; Melo et al., 2018).

The loss of vegetation removes the mechanical and hydrological stabilising effects activated by roots and foliage (MacDonald, 2004; Cerdà, 1998; Larsen et al., 2009). Roots generally act as mechanical reinforcement aiding the slope to cope with the drop in shear strength occurring when rainfalls increase pore-water pressures in the subsoil (Yuan-jun et al., 2022, Bordoloi et al., 2020). Following a wildfire, roots progressively disappear over time at a rate that depends on fire severity and root type (Gehring et al., 2019). Fine roots are expected to fail rapidly, whereas structural roots may continue reinforcing the subsoil for a period of time. The growth of new vegetation and root systems may or may not offset the progressive loss of old roots depending on the type of plants involved (Vergani et al., 2017).

Slope stability also benefits from hydrological effects induced by vegetation (Cerdà et al., 2008, Rengers et al., 2020) that a wildfire abruptly turns off. The first negative occurrence is the loss of rainfall interception by the canopy and the consequent increase of the amount of rainfall falling on the slope. Another effect is the vanishing of root water uptake induced by transpiration (Gerrits et al., 2010). Although soil evaporation continues, this is a superficial process much less effective than transpiration in desaturating the subsoil.

A wildfire can affect this superficial evaporation because a few centimetres of a Wooden Embers Cover (WEC) replace vegetation on the slope surface. The WEC has hydraulic and thermal properties that differ from those of the subsoil and can affect rainfall infiltration and evaporation to an extent that is still poorly investigated in the literature. It has been suggested that the subsoil decreases water retention after a wildfire due to the WEC formation (Ebel et al., 2016). However, the fundamental thermo-hydraulic mechanisms leading to the reduced water storage capacity have not been elucidated, nor have their consequences on slope stability.

The original research questions addressed by this paper are i) whether a WEC replacing vegetation following a wildfire can alter the hydrological behaviour of the slope due to its different thermohydraulic properties compared to the subsoil and ii) to what extent these changes can predispose silty volcanic soil slopes (SILT) to rainfall-induced instability. These questions are investigated both experimentally and numerically.

A physical model (lysimeter) (Rianna et al., 2012) consisting of a one-cube meter-sized wooden tank was filled with SILT and placed outdoors for several years to investigate the soil-atmosphere interaction, initially under bare conditions over four years (no-WEC-bare conditions), followed by five years of vegetated cover (no-WEC-vegetated conditions), and finally with a 5 cm-thick WEC placed on top of the SILT for four years, after removing the vegetated layer (SILTWEC conditions). The hydrological effect induced by WEC was assessed by comparing the response of SILTWEC against bare and vegetated conditions with no WEC. As the WEC was placed at environmental temperature, the impact of high temperatures on SILT topsoil, including a reduction in soil aggregate stability and changes in soil water repellence (Shakesby et al., 2006; Letey, 2001) could not be reproduced. Numerical modelling of the coupled thermohydraulic flow generated by the atmospheric variables was developed to support data interpretation.

Finally, the practical consequences of a WEC forming on a silt slope were investigated numerically by considering the case study of the 2005 rainfall-induced landslide that occurred in Nocera Inferiore, Italy (Pagano et al., 2019). The slope is made of the same SILT tested in the lysimeter. Its response to meteorological variables recorded at the landslide site was reanalysed by simulating the presence of a WEC with the same thermohydraulic properties as the material tested in this study.

2. Physical model

Figure 1 shows a schematic layout of the physical model (lysimeter), in the version upgraded to carry out the present study. The original physical model consisted of a 0.75 m thick SILT of volcanic origin in a wooden tank (Rianna et al., 2014b). The SILT was collected in Nocera Inferiore (Italy) from the site where a rainfall-induced shallow landslide occurred on 4 March 2005. The SILT was placed using the pluvial deposition technique to reproduce the high porosity encountered in the field (70%), as detailed by Olivares & Picarelli (2003). Details about the monitoring system, including meteorological variables and soil hydraulic and thermal status variables, can be found in Rianna et al. (2014b).

The SILT had been tested for four years under bare conditions (Rianna et al., 2014b) and with a grass-vegetated cover over the subsequent five years (Pagano et al., 2019). For the present study, a 5 cm-thick WEC layer was placed on top of the SILT after removing the vegetation and maintained for three years. Additional instruments were added to the WEC, including small tip tensiometers, heat dissipation suction probes to monitor matric suction, and thermistors to monitor temperature.

Coppola, L., Reder, A., Rianna, G., Tarantino, A., & Pagano, L. (in press). Effects of Wooden Embers Cover on thermo-hydrological response of silty volcanic cover and implications to post-wildfire slope stability. *Engineering Geology*.

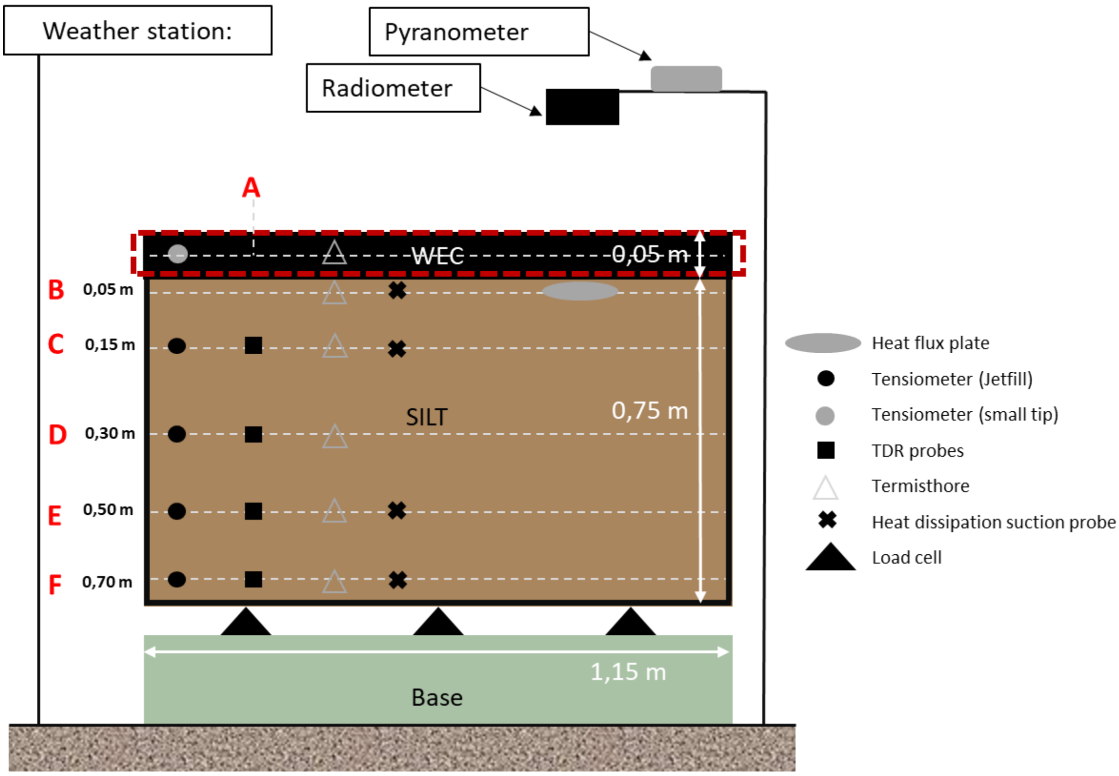

Figure 1. Physical model (lysimeter) adopted to study the soil-atmosphere interaction of the SILT layer under bare, vegetated, and wooden embers-covered conditions

3. Materials and thermo-hydraulic characterisation

Figure 2 shows the grain size distribution of SILT and WEC materials. The SILT is a volcanic sandy silt generated by the Plinian volcanic eruption of Vesuvius volcano in 79 AD. The WEC is a gravelly-silty-sand obtained by burning strawberry tree wood. Both materials have no plasticity due to the high temperatures to which they were exposed during their genesis. In the physical model, these materials were emplaced at high porosity, 73% for the SILT and 80% for the WEC. Corresponding dry unit weights were 7 and 4.8 kN/m^3, respectively. The specific gravity is 2.6 and 2.4 for the SILT and WEC, respectively.

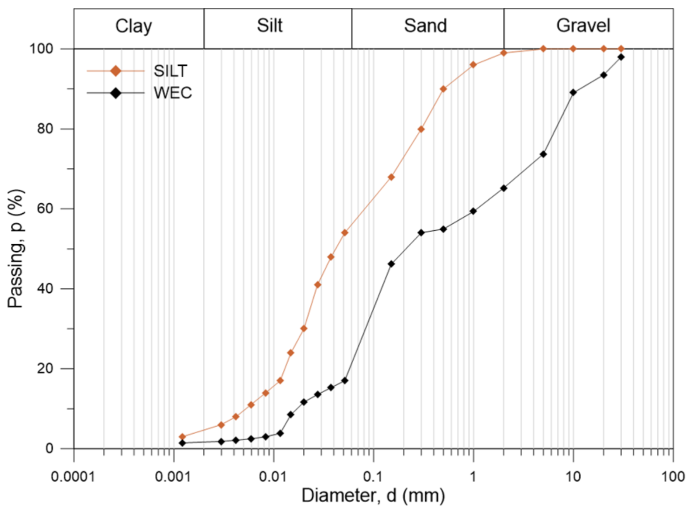

Figure 2. Grading curves of SILT and WEC materials

Figure 3 shows the main drying water retention curves determined experimentally and modelled by the Van Genuchten equation (1980) (parameters in Table 1, curves provided in supplementary data):

$$\theta = \theta_r + (\theta_s - \theta_r)\left[\frac{1}{1+(\alpha s)^n}\right]^m \qquad [1]$$

where θ is the volumetric water content, *s* is the suction, θ_s and θ_r are the saturated and residual volumetric water contents, respectively, and α, *n*, and *m* are soil parameters. The SILT curve was derived by monitoring simultaneously suction and volumetric water content in the bare SILT (Rianna et al., 2014b). The WEC water retention curve was determined on laboratory specimens initially subjected to full saturation and then desaturated in steps by air-drying. At each drying stage, specimens were weighed to back-calculate water content from the specimen's final mass, while suction was measured using a small tip tensiometer. The Air-Entry Value (AEV) of WEC and SILT were 4 kPa and 12 kPa, respectively. At 80 kPa (tensiometer full-scale range), the WEC water content, θ_{80}, was equal to 0.2, lower than the value measured for the SILT (θ_{80}=0.30).

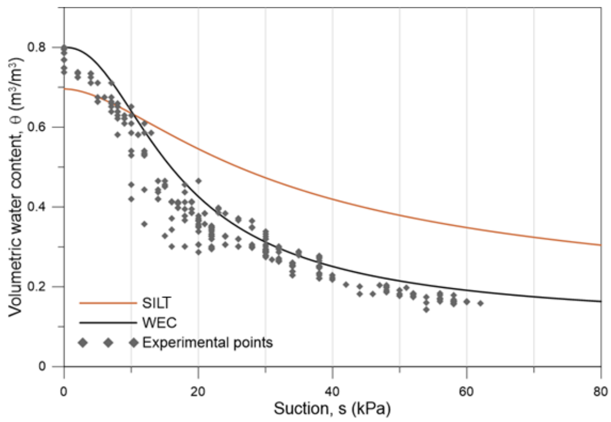

Figure 3. Soil Water Retention Curves for SILT and WEC

Table 1. Hydraulic parameters for SILT and WEC materials

	SILT	WEC
θ_{sat} (m^3/m^3)	0.70	0.80
θ_{res} (m^3/m^3)	0.10	0.10
α (1/kPa)	0.049	0.080
n (-)	1.756	2.260
m (-)	0.431	0.560
k_{sat} (m/s)	3×10^{-6}	3×10^{-5}

Coppola, L., Reder, A., Rianna, G., Tarantino, A., & Pagano, L. (in press). Effects of Wooden Embers Cover on thermo-hydrological response of silty volcanic cover and implications to post-wildfire slope stability. *Engineering Geology*.

The hydraulic conductivity at saturation of the WEC was measured on three specimens tested in a constant head permeameter under a hydraulic head differential of 5 cm, which returned hydraulic conductivity values of k_{sat}^{WEC}=3.0, 3.1, and 3.0 × 10^{-5} m/s respectively. For SILT, the hydraulic conductivity at saturation was derived via the joint transient measurement of suction and water content in the lysimeter, k_{sat}^{SILT} =3.0 × 10^{-6} m/s (Rianna et al., 2014b). The unsaturated hydraulic conductivity function for both materials (Figure 4) was determined through inverse analysis of the evolution of suction and water content along a desaturation path (in the lysimeter for the SILT and the specimens for the WEC), according to the procedure proposed by Nicotera et al. (2010), which is based on the numerical solution of the water flow Richards' equation. The inverse analysis was carried out by using the Mualem-Van Genuchten (1980) model, i.e., Eq. [1] for the water retention function and the following equation for the hydraulic conductivity function:

$$k = k_{sat}\sqrt{\theta_e}\left[1-\left(1-\theta_e^{\frac{1}{m}}\right)^m\right]^2 \qquad \left[\theta_e = \frac{\theta-\theta_r}{\theta_s-\theta_r}\right] \qquad [2]$$

where k_{sat} is the hydraulic conductivity at saturation and θ_e is the effective degree of saturation. At full saturation, the WEC hydraulic conductivity (k_{sat}^{WEC}=10^{-5} m/s) is one order of magnitude higher than that of the SILT (k_{sat}^{SILT} =10^{-6} m/s). The hierarchy between hydraulic conductivities reverses for suction exceeding 30 kPa. At 50 kPa, the WEC hydraulic conductivity (k_{50}^{WEC}=10^{-11} m/s) is already one order of magnitude lower than that of the SILT (k_{50}^{SILT} =10^{-10} m/s). The gap increases by two orders of magnitude at 100 kPa, (k_{100}^{WEC}=10^{-12} m/s; k_{100}^{SILT} =10^{-10} m/s) and four orders of magnitude at 300 kPa (k_{300}^{SILT}=10^{-15} m/s, k_{300}^{WEC} =10^{-11} m/s).

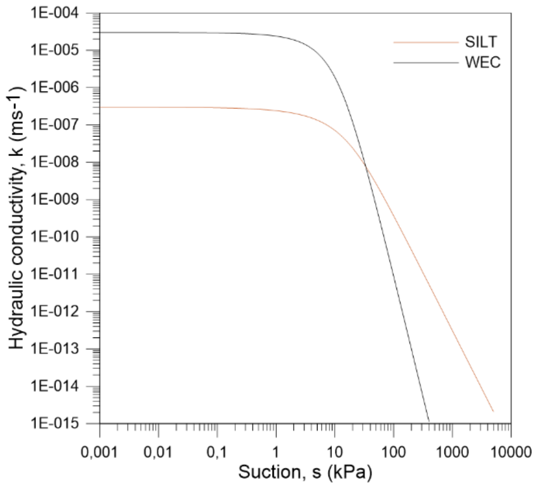

Figure 4. Hydraulic conductivity functions for SILT and WEC, obtained by back-analysing the evolution of suction and water content along a desaturation path

The thermal properties (thermal conductivity, λ, and volumetric specific heat, c_v) were quantified experimentally at different volumetric water contents. The thermal conductivity for the WEC and the SILT, λ^{WEC} and λ^{SILT} respectively, was obtained from lysimeter data, interpreting measurements by heat dissipation probes installed in WEC and SILT layers according to the equation proposed by Shiozawa & Campbell (1990). This equation relates λ to the heat (q_t) supplied to the probe per unit length, the time Δt during which q_t is supplied, and the temperature change, ΔT, that q_t induces in the probe:

$$\lambda = \frac{q_t}{4\pi\Delta T}\ln(\Delta t) \qquad [3]$$

The volumetric water content in the SILT was measured by TDR installed at 15 cm below the SILT uppermost surface (Rianna et al., 2014a). The volumetric water content in the WEC was inferred from suction measurements and its water retention curve.

The thermal conductivity functions for the WEC and the SILT, respectively, are presented in Figure 5 and show that λ^{WEC} remains markedly higher than λ^{SILT} at any volumetric water content. The thermal conductivity λ was modelled using the following equation (parameters listed in Table 2)

$$\lambda = \lambda_1 + \alpha_1 \exp(b_1\theta) \qquad [4]$$

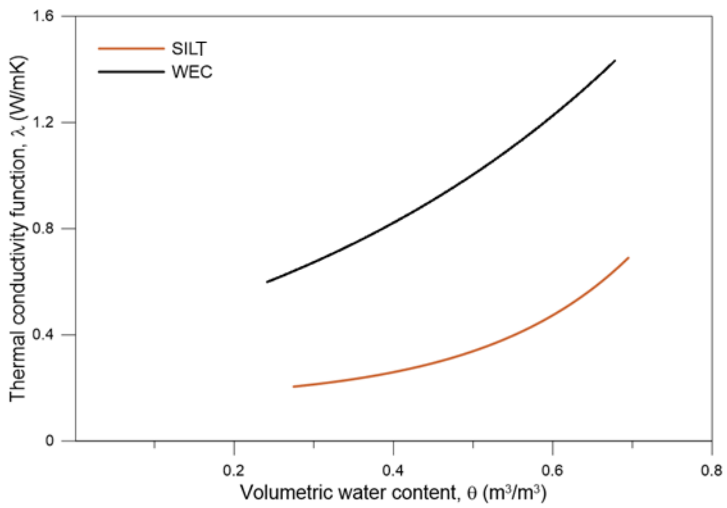

Figure 5. Thermal conductivity functions for SILT and WEC

The volumetric specific heat function, $c_v^{WEC}(\theta)$ for the WEC layer was derived by the formula proposed by de Vries (1963), which quantifies this parameter by weighting the (known) volumetric specific heat of solid, c_s, and liquid, c_w, matrixes respectively according to their densities and volumetric fractions:

$$c_v^{WEC} = \varphi_s c_s \rho_s + \varphi_w c_w \rho_w \qquad [5]$$

where φ_s and φ_w are the volumetric fractions of the solid matrix ($\varphi_s = 1-\theta_{sat}$) and the liquid matrix ($\varphi_w = \theta_{sat}$), respectively, and ρ_s and ρ_w are the densities of the solid matrix and liquid matrix, respectively (parameters in Table 2).

The volumetric specific heat function, $c_v^{SILT}(\theta)$ for the SILT layer was obtained by inverse analysis of heat flux in the SILT in the physical model based on a triplet of temperature measurement points (Reder et al., 2018) and modelled using the equation:

$$c_v^{SILT} = c_{h0} + a_0 \exp(b_0 \theta) \quad [6]$$

where c_{h0}, a_0, and b_0 are fitting parameters (Table 2).

For both materials, the volumetric specific heat increases with increasing water content (Figure 6), linearly for the WEC, and more than linearly for the SILT. The specific heat for the WEC, $c_v^{WEC}(\theta)$, is markedly higher than the one for the SILT, $c_v^{SILT}(\theta)$, i.e., the WEC has higher capacity for heat storage. Thermal parameters for WEC and SILT are reported in Table 2.

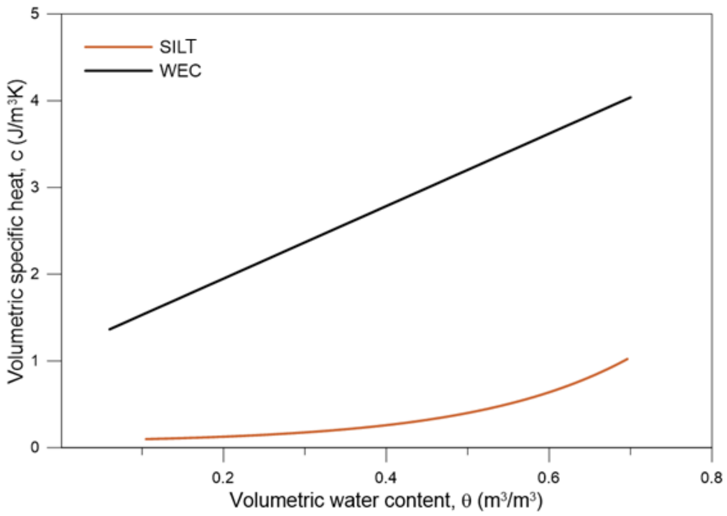

Figure 6. Volumetric specific heat functions for SILT and WEC

Table 2. Thermal parameters for SILT and WEC

Volumetric specific heat function					
WEC	*c_s (MJ/m^{3}K) - WEC*	2.31*	**SILT**	*c_{h0} (J/m^3 K)*	0.055
	ρ_s (g/cm^3)	2.41			
LIQUID MATRIX	*c_w (MJ/m^{3}K)*	4.186		*a_0 (J/m^3 K)*	0.025
	ρ_w (g/cm^3)	1		*b_0 (-)*	5.252
Thermal conductivity					
WEC	*λ_1 (W m K^{-1})*	0.148	**SILT**	*λ_1 (W m K^{-1})*	0.897
	α_1 (W m K^{-1})	0.013		*α_1 (W m K^{-1})*	0.3697
	b_1 (–)	5.406		*b_1 (–)*	1.9974

(*) Waples and Waples, 2004)

The capacity of a material to transmit temperature variations depends on its thermal diffusivity α, which decreases with decreasing thermal conductivity and increasing volumetric specific heat ($\alpha = \lambda / c_v \rho_s$). The SILT thermal diffusivity function $\alpha^{SILT}(\theta)$ is nearly independent of volumetric water content and is placed well below the WEC function $\alpha^{WEC}(\theta)$, which decreases sharply with increasing volumetric water content (Figure 7). In short, although characterised by a higher thermal conductivity, the WEC is less prone to transmit heat thanks to its heat storage capability. The gap with the SILT reduces at high volumetric water contents.

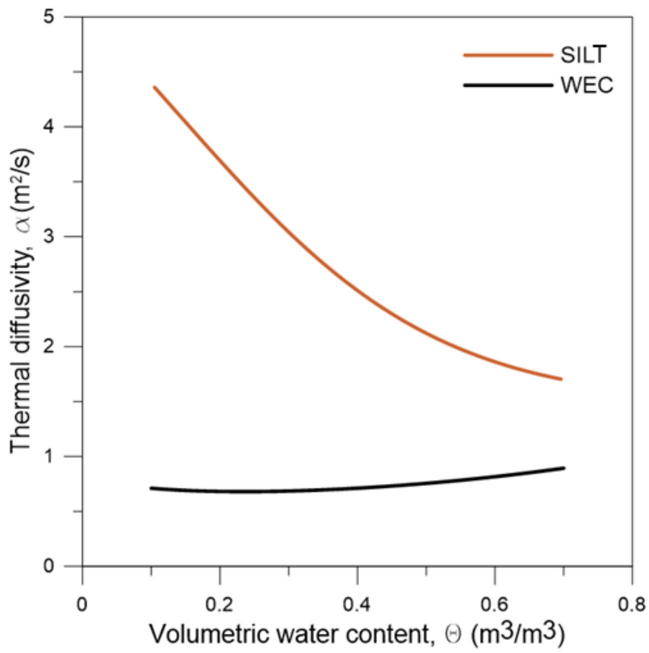

Figure 7. Comparison between SIL and WEC thermal diffusivities functions

4. Monitoring results

This section presents the hydrological (water storage, volumetric water content, suction) and thermal (temperature) response of the lysimeter under SILTWEC conditions (silt layer covered by wooden embers). Measurements are presented separately for the SILT layer (§4.1) and WEC layer (§4.2). Measurements carried out in the SILT layer in the period 2019-2022 are plotted in comparison with measurements previously detected under bare condition, i.e., no WEC cover (2010-2014, Rianna et al., 2014a) and vegetated condition (2014-2019, Pagano et al., 2019).

4.1 Thermal and hydrological response of the SILT layer under SILTWEC conditions (in comparison with bare and vegetated conditions)

4.1.1 Suction and volumetric water content

Figure 8 plots the evolution of the average volumetric water content quantified by weighing the lysimeter. The brown curve refers to SILT layer alone under no-WEC-bare conditions, the green curve to the SILT layer alone tested after sowing vegetation (no-WEC-vegetated conditions), and the grey curve to the WEC overlying the SILT layer (SILTWEC).

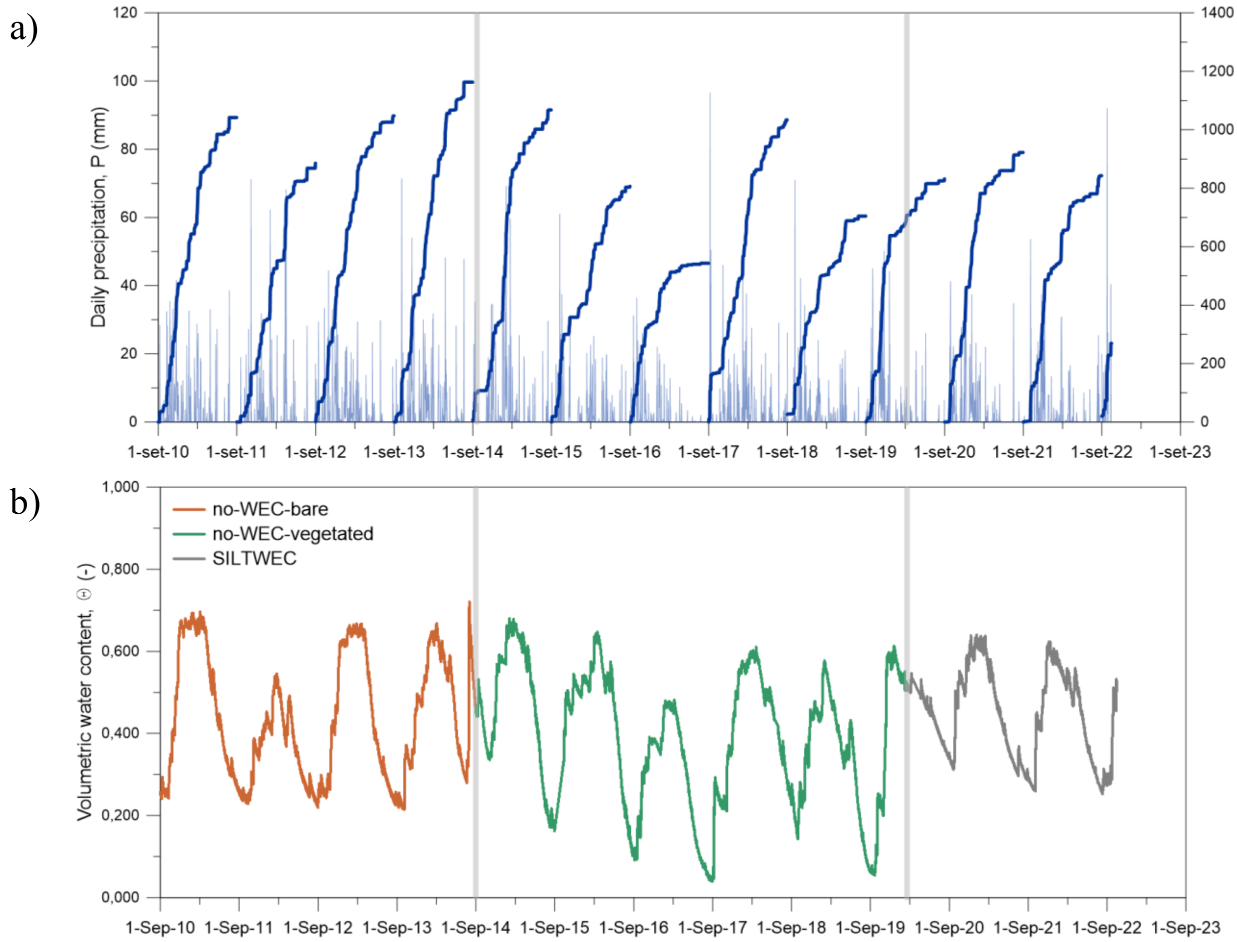

Figure 8. Measurements from September 2010 to August 2023 (a) Daily and yearly cumulated rainfall. (b) Water storage computed from measurements of lysimeter total weight (data for no-WEC-bare after Rianna et al., 2014b; data for no-WEC-vegetated after Pagano et al., 2019).

Under all covering conditions, it may be observed that the average volumetric water content often stabilises at a "wet threshold" during the wet period (Rianna et al., 2014b). This threshold is controlled by the drainage occurring at the bottom of the lysimeter when pore-water pressures at the bottom attain zero or slightly positive values, preventing any further increase in the amount of water stored in the soil (Rianna et al., 2014b). The wet threshold observed at ~0.7 m^3/m^3 volumetric water content is directly associated with the SILT porosity. Volumetric water content lowers during the dry season due to evaporation (or evapotranspiration for the vegetated cover) prevailing on rainfall infiltration. A different minimum is reached over the drying period ("dry threshold") for the three covering conditions. As expected, the dry threshold is lower in the presence of vegetated cover due to 'distributed' water uptake by roots as opposed to evaporation taking place from the surface for the case of bare and WEC conditions. It is worth noting that the "dry threshold" (0.25 m^3/m^3) in the presence of WEC is higher than the one observed under bare conditions (0.20 m^3/m^3).

Figure 9a compares the evolution of volumetric water content for three selected hydrological years characterised by different covering conditions but similar potential evaporation/evapotranspiration evolution during the dry periods as shown in Figure 9b (curves for the three selected hydrological years are overlapped in the same graph). The selected hydrological years are September 2012-August 2013 for the bare soil (3rd year), September 2015-August 2016 for vegetated soil (6th year), and September 2020-August 2021 for the SILT+WEC (11th year). Starting from similar volumetric water content levels at the end of the wet season, the decay in water storage differs for the three surface covers (bare, vegetated, and WEC) although driven by similar meteorological forcing. The decay in water storage is gentlest for the case of the WEC trend and steepest for vegetated cover, leading to substantially different dry thresholds.

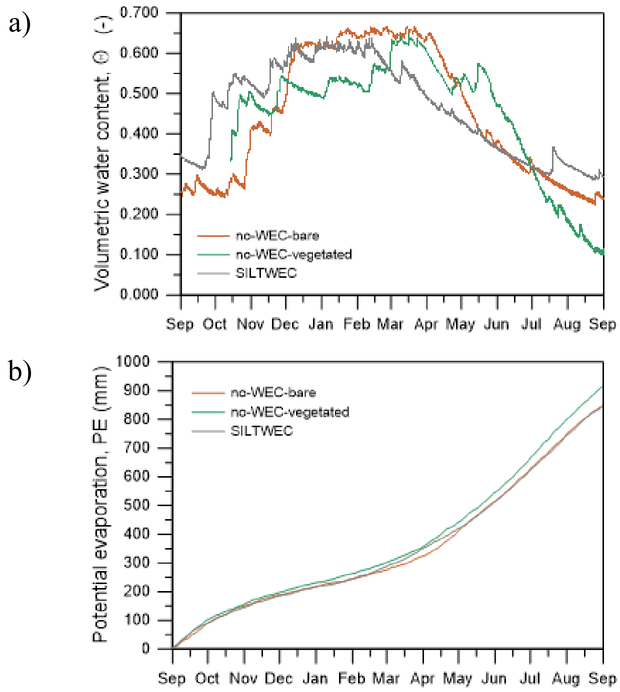

Figure 9. Three distinct hydrological years (3rd, 6th and 11th), each characterised by a different covering condition but similar evolution of potential evaporation/evapotranspiration (curves are overlapped in the same graph). (a) Global volumetric water content. (b) Evaporation/evapotranspiration (data for no-WEC-bare after Rianna et al., 2014b; data for no-WEC-vegetated after Pagano et al., 2019).

Figure 10 plots the suction and volumetric water content evolution monitored at four depths as indicated in Figure 1. Suction fluctuates over time consistently with weather conditions, reducing to a few kPas over wet periods and increasing to tens of kPa over dry periods.

During the dry period, suction tends to increase more under vegetated soil conditions than under bare soil conditions, especially at depths greater than 15 cm. Differences between vegetated and bare conditions are due to the water uptake by roots throughout the SILT, which enhances desaturation far from the soil surface (Pagano et al., 2019). For these two covering conditions, suction exceeds the tensiometers full scale of 80 kPa around the middle of the dry period in any hydrological year. When this occurred, tensiometers were re-saturated to enable suction monitoring during the following wet period.

In the presence of WEC, suction observed over the wet periods shows a similar pattern to that observed for bare and vegetated cover. Suction evolution observed for the case of WEC at any depth departs during the dry seasons because of reduced water loss by evaporation. Suction remains relatively low during the dry period to the point that the tensiometer measurement range is not exceeded, ensuring continuity of tensiometer measurements over the transition from dry to wet periods.

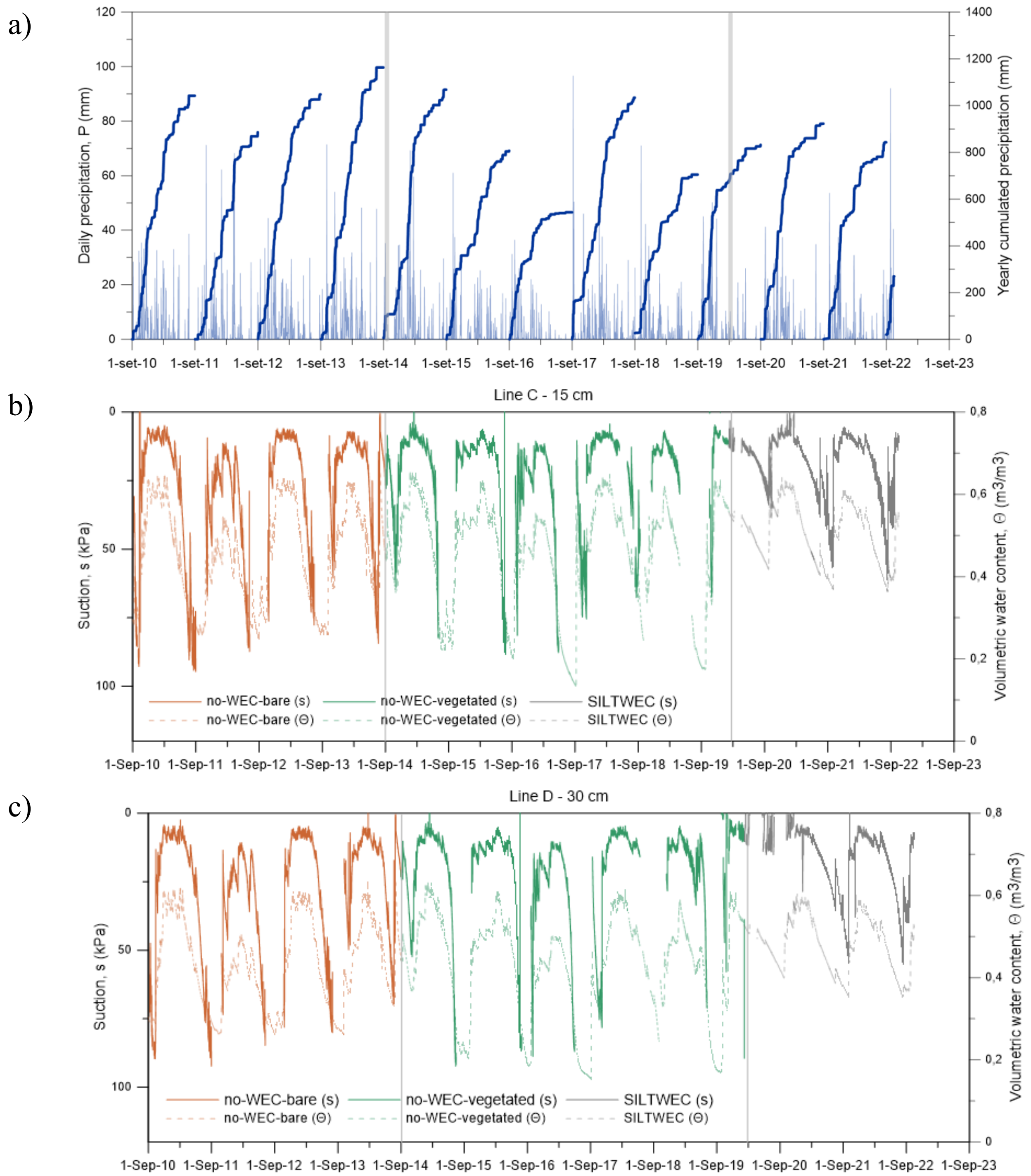

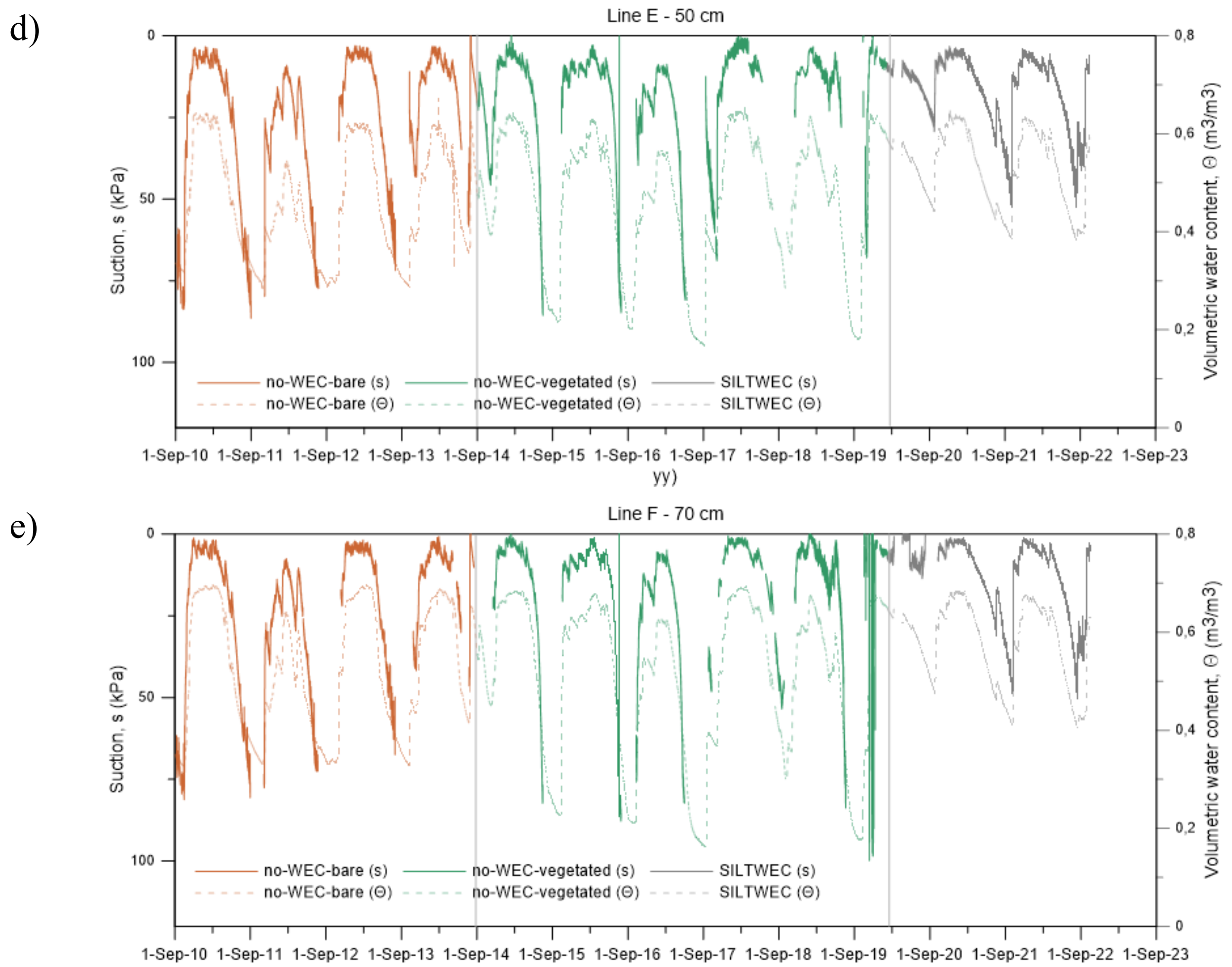

Figure 10. Measurements from September 2010 to August 2023. (a) Daily and yearly cumulated rainfall. (b), (c), (d), and (e) Suction and volumetric water content measured at Line C-15 cm, Line D-30 cm, LineE-50 cm, and Line F-70 cm respectively (data for no-WEC-bare after Rianna et al., 2014b; data for no-WEC-vegetated after Pagano et al., 2019).

Water content measured using TDR probes installed at the same depth as the tensiometers shows patterns consistent with the suction measurements (Figure 10). Under all covering conditions, volumetric water content observed over the wet periods attains a threshold at θ=~0.65, slightly lower than the value at full saturation (θ_{sat}=~0.7). During the dry season, the evolution of water content diverges substantially for the three covering conditions reflecting the variations in global water storage as presented in Figure 8 and Figure 9. The different desaturation trends observed for the three different covering conditions determine three different dry minima for the volumetric water content, ~0.4 for WEC, ~0.25 for vegetated, and ~0.35 for bare conditions.

Figure 11 displays water content-suction data points recorded at the four monitored depths to represent the water retention behaviour of the SILT. The water retention behaviour appears to have remained very stable over the 12-year period regardless of the covering conditions.

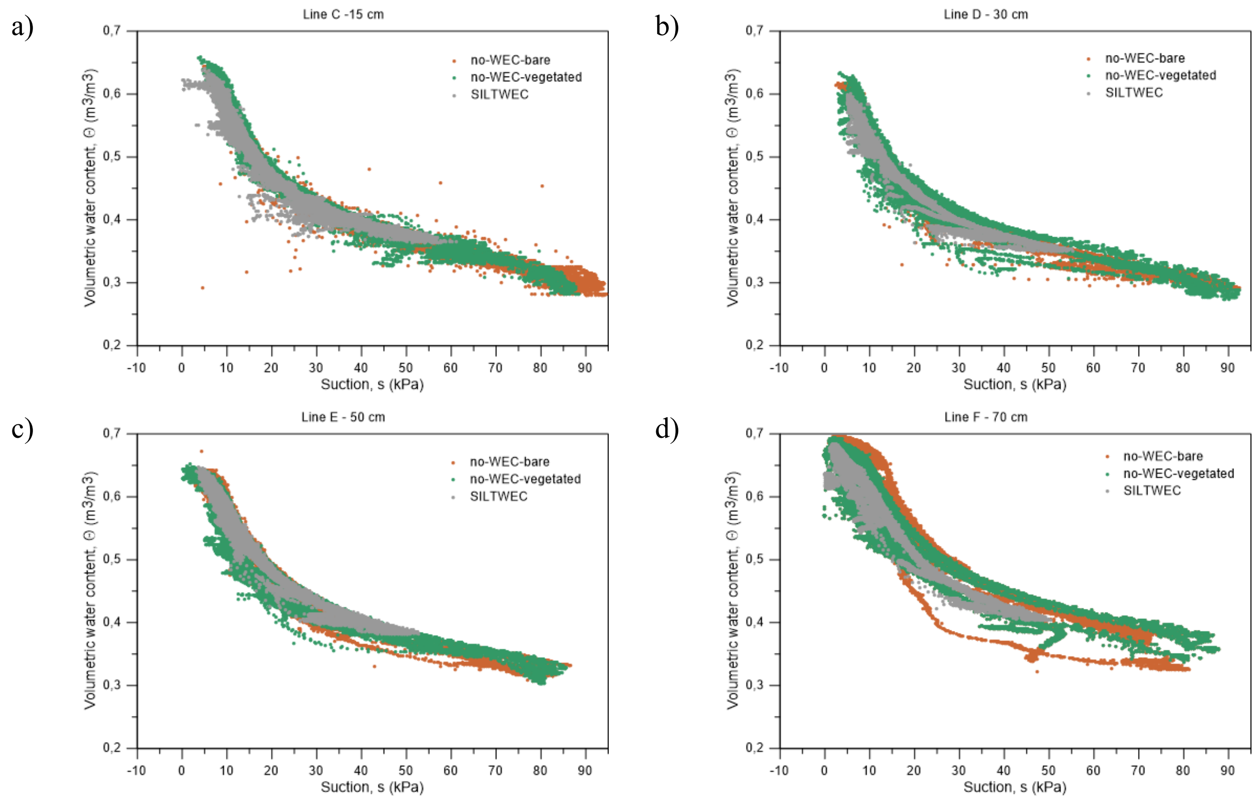

Figure 11. Water content-suction datapoints measured at Line C-15 cm (a), Line D-30 cm (b), LineE-50 cm (c), and Line F-70 cm (d) respectively

4.1.2 Temperature

Three hydrological years, the 2nd (no-WEC-bare conditions), the 6th (no-WEC-vegetated conditions), and the 11th (SILTWEC conditions) year were selected to illustrate the effect of covering condition on SILT thermal response. The air temperature evolutions were sufficiently similar to make it possible to associate differences in SILT thermal response with the type of covering.

It should be noted that a 5 cm thick WEC was added on the top of the SILT. As a result, the shallowest thermistor of line *B* (Figure 1) was 5 cm depth under no-WEC-bare and no-WEC-vegetated conditions and 10 cm depth under SILTWEC conditions. The difference in depth from the surface also applies to the second shallower thermistor *C* (10 cm depth under bare/vegetated conditions, 15 cm depth under WEC).

Figure 12a,b plots the average hourly air temperature over a day, computed by averaging the hourly temperature over one trimester in the hot season (Jun-Jul-Aug, Fig. 12a) and in the cold season (Jan-Feb-Mar, Figure 12b) for the 2nd (no-WEC-bare condition), 6th (no-WEC-vegetated condition), and 11th (SILTWEC condition) year.

Figure 12c,d shows the temperature recorded by the thermistor for the line B (at 10 cm depth under SILTWEC conditions) compared with the temperature simulated at 10 cm depth under no-WEC-bare/vegetated covering by interpolating the temperatures measured at 5cm depth (line B) and 15 cm depth (line C) according to the approach presented by Rianna et al. (2014a) based on the heat transmission equation under 1D condition

Coppola, L., Reder, A., Rianna, G., Tarantino, A., & Pagano, L. (in press). Effects of Wooden Embers Cover on thermo-hydrological response of silty volcanic cover and implications to post-wildfire slope stability. *Engineering Geology*.

(Hillel, 2003; Marshall et al., 1996). This figure shows clearly that the WEC dampens temperature fluctuations at the same depth compared to bare/vegetated covering.

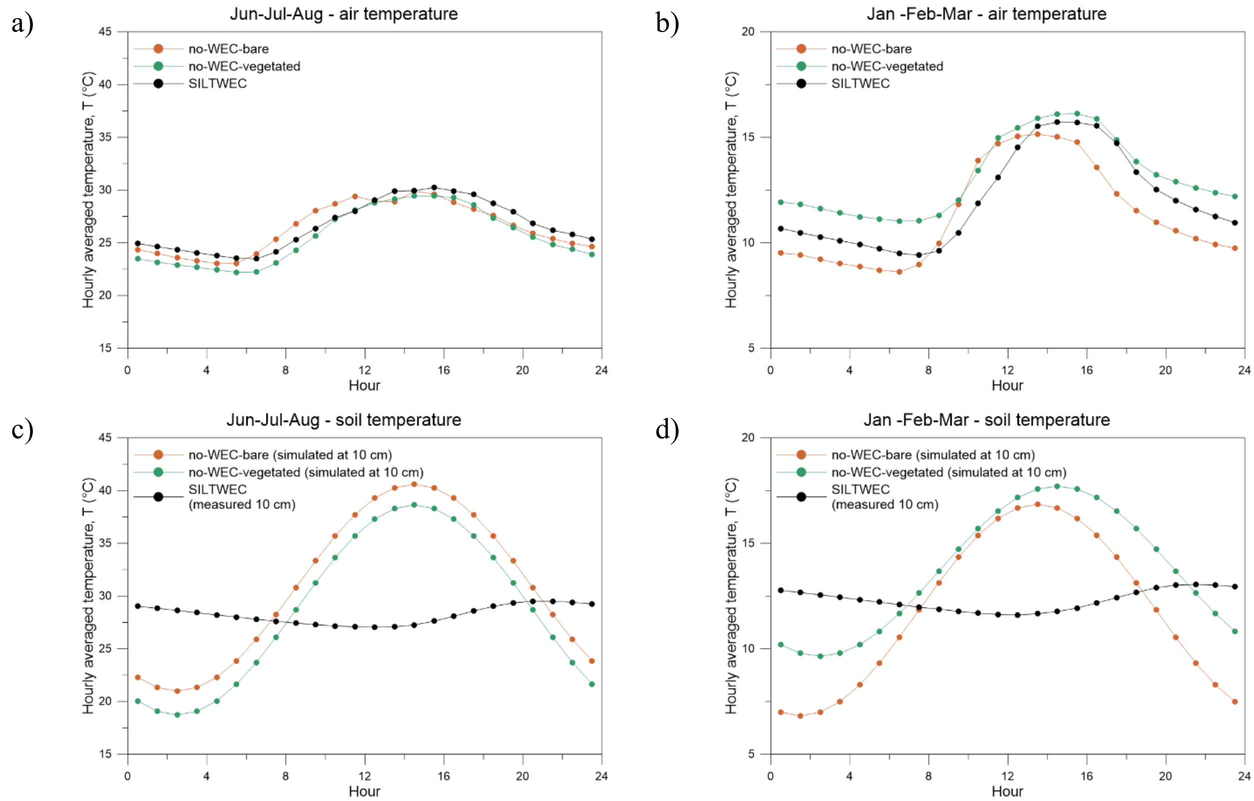

Figure 12. Average hourly air temperature over a day, computed by averaging the hourly temperature over one trimester for the 2nd (bare condition), 6th (vegetated condition), and 11th (WEC condition) years. (a) Measured air temperature in the hot season (Jun-Jul-Aug). (b) Measured temperature in the cold season (Jan-Feb-Mar). (c) Measured temperature in SILT+WEC against simulated temperature in bare and vegetated SILT in the hot season (Jun-Jul-Aug). (d) Measured temperature in SILT+WEC against simulated temperature in bare and vegetated SILT in the cold season (Jan-Feb-Mar).

4.2 Thermal and hydrological response of the WEC layer

A small-tip tensiometer and a heat dissipation probe to monitor matric suction were installed in the middle of the WEC layer (line A Fig. 1). Figure 13 plots the suction evolution in the WEC layer over the last three years of the experiment. Suction never drops below 5 kPa, ranging between this minimum value and 30 kPa for most of the year. In the middle of the dry season, suction abruptly exceeds the tensiometer full-scale range with the consequent measurement interruption.

Coppola, L., Reder, A., Rianna, G., Tarantino, A., & Pagano, L. (in press). Effects of Wooden Embers Cover on thermo-hydrological response of silty volcanic cover and implications to post-wildfire slope stability. *Engineering Geology*.

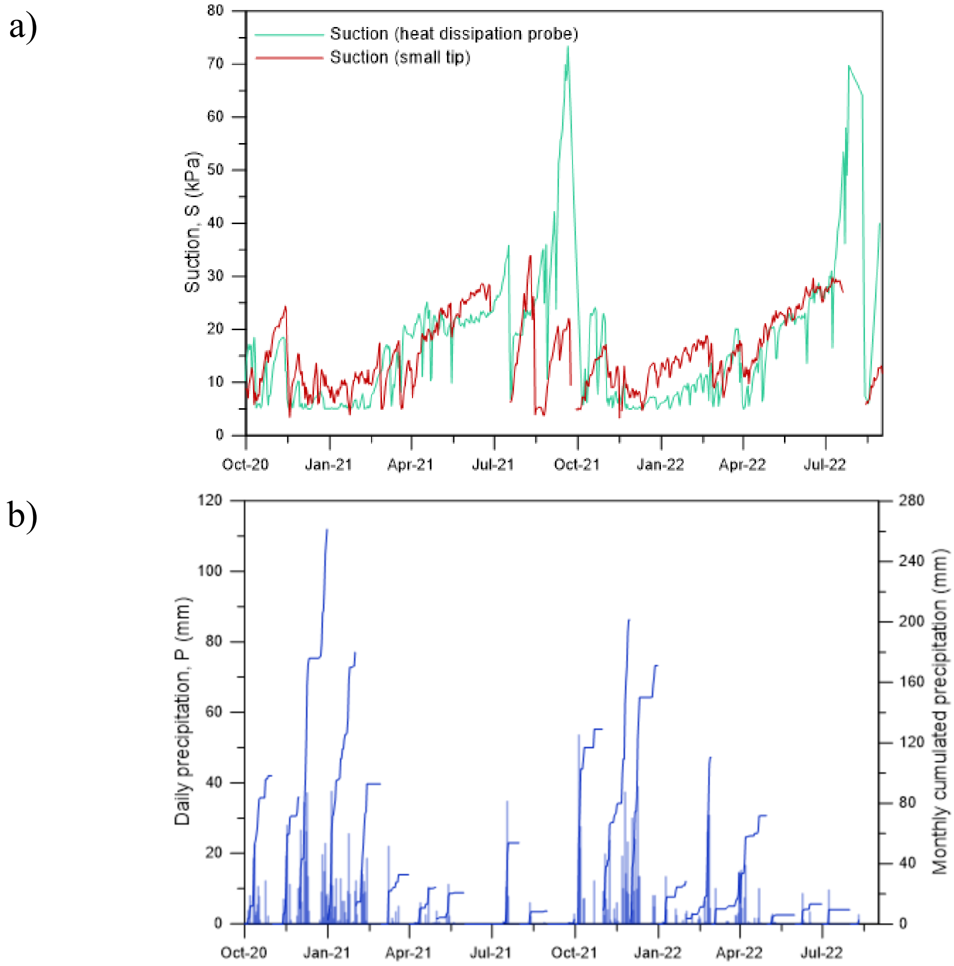

Figure 13. (a) Suction evolution measured within the WEC layer (line A); (b) daily and monthly cumulated precipitations.

Figure 14 shows the average hourly temperature of air, WEC (line A) and SILT (line B) computed over the two considered trimesters. The WEC temperature fluctuates according to the air temperature. During the dry-hot period, the temperature in the WEC exceeds the air temperature while the temperature in the SILT remains markedly below the air temperature in the central part of the day, implying that the WEC becomes hotter while storing the heat supplied by the atmosphere without transmitting it to the SILT layer.

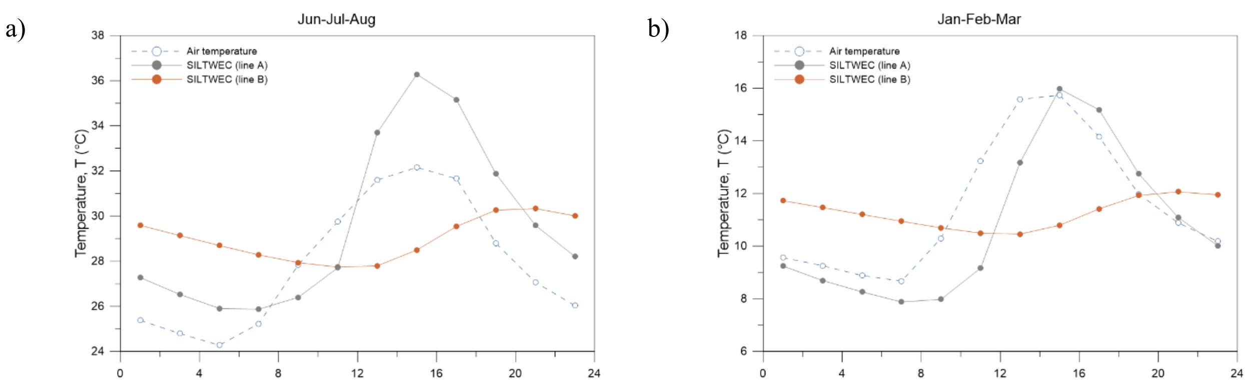

Coppola, L., Reder, A., Rianna, G., Tarantino, A., & Pagano, L. (in press). Effects of Wooden Embers Cover on thermo-hydrological response of silty volcanic cover and implications to post-wildfire slope stability. *Engineering Geology*.

Figure 14. Comparison between evolutions of air and soil temperature (SILT and WEC) during a) June-July-August (Jun-Jul-Aug), b) January, February-March (Jan-Feb-Mar).

5. Numerical simulation of hydrological and thermal response of physical model

5.1 Governing equations

The coupled thermohydraulic approach proposed by Wilson (Wilson et al., 1994) has been adopted to analyse the response of a two-layer system to the atmospheric variables. Similar approaches have been successfully adopted to investigate embankment stability (Gitirana, 2005), soil-structure interaction (Al Qadad et al., 2012), and soil-water budget (Cui et al. 2005).

Wilson's approach includes the water balance equation, the heat balance equation, and thermodynamic phase equilibrium as the governing equations.

The water balance equation is expressed as:

$$\frac{1}{\rho_w g}\frac{\partial(u_a - u_w)}{\partial t} = \frac{1}{\rho_w g m_2^w}\left[\frac{\partial}{\partial z}\left(k_w + \frac{k_w}{\rho_w g}\frac{\partial(u_a - u_w)}{\partial z}\right) + \left(\frac{P_a + u_v}{P_a \rho_w}\right)\frac{\partial}{\partial z}\left(D_v \frac{\partial u_v}{\partial z}\right)\right] \quad [7]$$

where u_w (kPa) = liquid pore-water pressure, u_a (kPa) = pore air pressure, u_v (kPa) = partial pressure of vapour pore-water, m_2^w (kPa^{-1}) = slope of soil water retention curve (SWRC), P_a (kPa) = total atmospheric pressure, k_w (ms^{-1}) = hydraulic conductivity function (HCF), D_v (°C) = vapour diffusivity through the soil, ρ_w (kg m^{-3}) = liquid water density, g (m s^{-2}) = gravitational acceleration.

Compared with the traditional form of the water balance equation, describing the flow of liquid water through porous media, equation [7] contains an additional term (the second one in the square brackets) accounting for water flux in the water phase.

The heat balance equation is expressed as:

$$C_h \frac{\partial T}{\partial t} = \frac{\partial}{\partial z}\left(\lambda \frac{\partial T}{\partial z}\right) - L_v\left(\frac{P_a + u_v}{P_a}\right)\frac{\partial}{\partial z}\left(D_v \frac{\partial u_v}{\partial z}\right) \quad [8]$$

where T (°C) = soil temperature, C_h (J/m^3 °C) = volumetric specific heat, λ (W/m °C) = thermal conductivity, L_v (J/kg) = latent heat of water vaporisation. In this equation, the second term on the right-hand side accounts for the energy spent on water vaporisation and represents the coupling with the water balance equation.

The thermodynamic equilibrium between the liquid and vapour phases of water is expressed as:

$$u_v = u_{v0}\, exp\left[\frac{(u_a - u_w)M_w g}{RT}\right] \quad [9]$$

where u_{v0} (kPa) = saturated partial pressure of pore vapour, M_w (kg/mol) = water molecular weight, R (J/mol °C) = ideal gas constant.

5.2 Boundary conditions

The following boundary conditions were imposed to the model:

1) *Liquid water flux*. Rainfall-induced flux is simulated by imposing an inward flux equal to rainfall intensity as long as this condition generates pore-water pressure at the boundary that is less than zero. If this last condition is not satisfied, null-pore-water-pressure is imposed at the boundary. During no-rain periods, evaporation-induced flux is simulated by imposing an outward flux equal to the Actual Evaporation (AE), in turn, assumed to be equal to the product of Potential Evaporation (PE) times a reduction function *k:*

$$AE = k\,PE \qquad [10]$$

Potential Evaporation is quantified according to the FAO approach (Allen et al., 1998) that takes the various crop conditions into account thanks to the crop coefficient (k_{crop}) that transforms the potential evaporation from a reference surface (a hypothetical grass reference crop with prescribed crop height, surface resistance and albedo) into potential evaporation in relation to the actual surface:

$$PE = k_{crop} RE = k_{crop}\left[\frac{0.408\Delta\cdot(R_n - G) + \gamma\frac{900}{T_a + 273}u_{2m}(u_{v0}^a - u_v^a)}{\Delta + \gamma(1 + 0.34u_{2m})}\right] \qquad [11]$$

where PE [kg m^{-2} s^{-1}] is the potential evaporation rate, RE [kg m^{-2} s^{-1}] is the potential evaporation rate from a reference surface (hypothetical grass reference crop with prescribed crop height, surface resistance and albedo), k_{crop} (-) is the crop coefficient, T_a [°C] is the air temperature, u_{2m} [m/s] is the wind speed at 2 m above the surface of the ground, Δ [Pa °C^{-1}] is the slope of the saturation vapour pressure curve at the air temperature T_a, γ [Pa °C^{-1}] is the psychrometric constant at the air temperature T_a, R_n [W m^{-2}] is the rate of net radiation, G [W m^{-2}] is the soil heat flux. The reduction function k considers the drop in the water vapour pressure in the soil as suction increases as opposed to the case of the free water surface for which the original Penman equation was derived. The reduction function was modelled according to Wilson et al. (1997):

$$k = \frac{exp\left[\frac{(u_a - u_w)_s M_w g}{RT_s}\right] - RH}{1 - RH} \qquad \left[RH = \frac{u_v}{u_{v0}}\right] \qquad [12]$$

A seepage surface is applied at the bottom boundary to simulate the condition determined by the geotextile and the perforated tank bottom. This consists of zero flux provided this condition generates pore water pressures at the boundary less than zero; otherwise, zero pore-water pressure is imposed at the bottom boundary (Reder et al., 2017).

Coppola, L., Reder, A., Rianna, G., Tarantino, A., & Pagano, L. (in press). Effects of Wooden Embers Cover on thermo-hydrological response of silty volcanic cover and implications to post-wildfire slope stability. *Engineering Geology*.

2) *Vapour water flux*. A vapour pressure $(u_v)_s$ was imposed at the surface and derived from air relative humidity RH and air temperature T_a records. RH provides the ratio $(u_v)_s/(u_{v0})_s$, while T_a provides the partial pressure of the vapor phase under saturated conditions $(u_{v0})_s$ using the Tetens equation (Tetens, 1930).

3) *Thermal flux.* Temperature T_s at the surface is assumed to be equal to air temperature T_a measured two meters above the ground surface, in line with the approach followed by Wilson et al. (1997).

It is worth highlighting that the illustrated model incorporates evaporation as a superficial process and an internal process associated with the deepening of the water phase transition surface over dry and hot periods. The simulation was performed using an input/output hourly time step; moreover, the adaptive time stepping scheme proposed by Milly (1982) was adopted for the inner time step.

5.3 Soil parameters

The numerical analyses were based on the soil-water retention and hydraulic conductivity functions defined by Eqs. [1] and [2] (hydraulic parameters listed in Table 1 for SILT and WEC layers) and thermal functions defined by Eqs. [3], [4], and [5] (thermal parameters listed in Table 2 for SILT and WEC layers).

5.4 Results

Figure 15 compares measured and computed suction at the four recorded depths over the period where the WEC was in place. By considering the same soil properties and boundary conditions as per the physical model (hereafter referred to as "SILTWEC"), the simulation reproduces the observed behaviour satisfactorily. It is worth noting that the computed trend accommodates the low suction observed during the dry periods, which is associated with the presence of the WEC layer.

To quantify the effect of WEC explicitly, the WEC layer of 5 cm was removed in the numerical model and replaced with a SILT layer of equal thickness (referred to as "SILT80'). The results indicate that the suction in SILT80 increases dramatically due to the lack of the barrier effect associated with the WEC barrier.

The barrier to outward water fluxes generated by the WEC is associated with the specific thermohydraulic properties of WEC material. One further simulation was conducted to investigate whether the WEC acts as a thermal or hydraulic barrier. A material was designed with the hydraulic properties of the WEC and the thermal properties of the SILT (referred to as SILWECh). This deactivates possible thermal barrier effects in the WEC. Results indicate that the suction over the dry period with the SILTWECh top layer only slightly rises over the SILTWEC one, demonstrating that WEC mainly acts as a hydraulic barrier. This effect is associated with the lower hydraulic conductivity of the WEC compared to the SILT at high suction (>30 kPa), as shown in Figure 4, which makes the WEC top act as a capillary barrier.

Coppola, L., Reder, A., Rianna, G., Tarantino, A., & Pagano, L. (in press). Effects of Wooden Embers Cover on thermo-hydrological response of silty volcanic cover and implications to post-wildfire slope stability. *Engineering Geology*.

a)

b)

c)

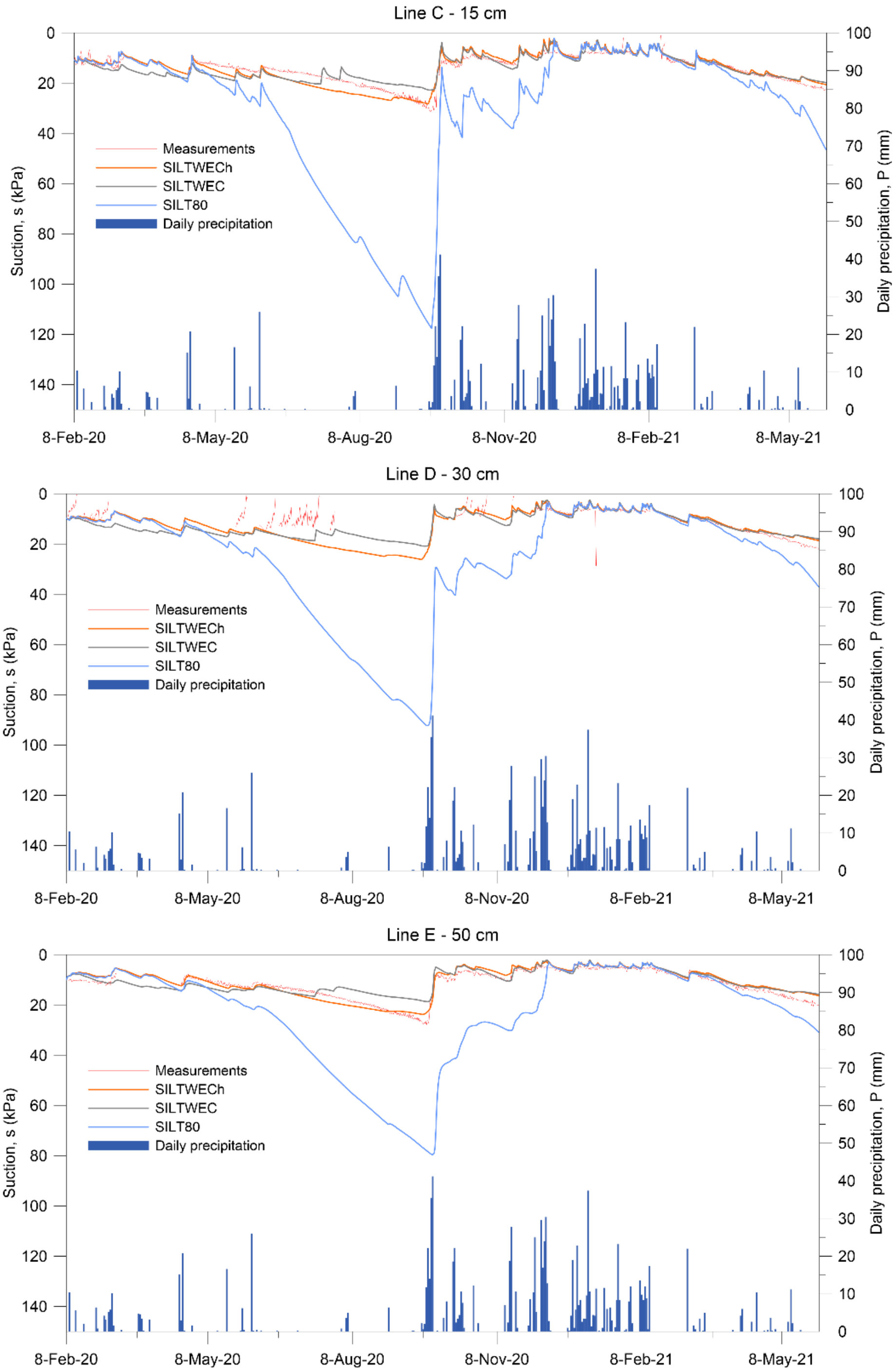

d)

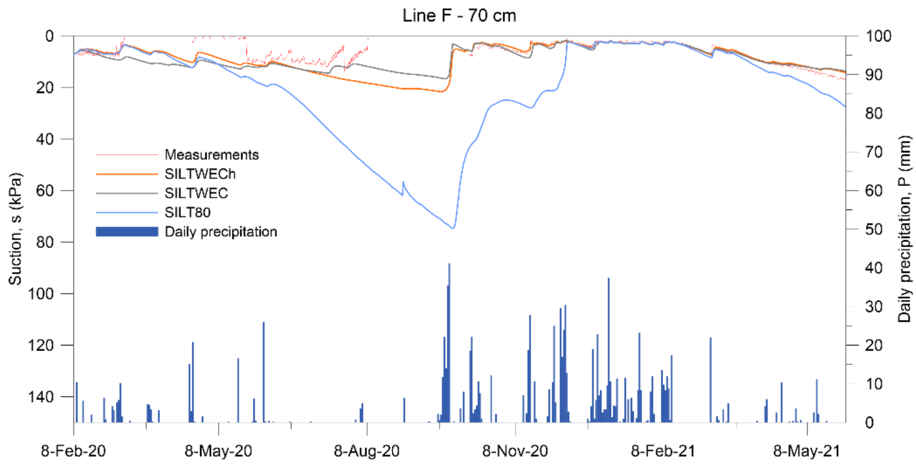

Figure 15. Comparison between measured and simulated suction at Line C-15 cm (a), Line D-30 cm (b), Line E-50 cm (c), and Line F-70 cm (d) respectively (grey curve = SILTWEC, physical model made of 75 cm of silt and 5 cm of WEC, each material has its own thermal and hydraulic properties; orange curve = SILTWECh, WEC layer has the thermal properties of the SILT; blue curve = SILT80, WEC layer replaced with SILT layer)

6. Implications of WEC formation on slope stability

The experimental results from the lysimeter tests and their numerical interpretation suggest that the formation of WEC following a wildfire could inhibit soil water fluxes induced by evaporation during the dry season, generating an increase in soil water content whose effect may extend to the subsequent wet season. Persistent lower suction levels during the wet season may reduce the severity of the rainfall events triggering slope instability, i.e., increase the slope's vulnerability to rainfall-induced failure. To demonstrate the potential quantitative impact of a WEC forming on a silt slope, the case study of the rainfall-induced landslide that occurred in 2005 in Nocera Inferiore, Italy (Pagano et al., 2010) was reanalysed by simulating the presence of a WEC following a wildfire and attributing to the WEC the same thermohydraulic properties of the material characterised in this study.

The evolution of suction and Factor of Safety (FoS) in the slope previously simulated under the scenarios of vegetated conditions (no-WEC) under the measured climatic loading was compared with the evolution of suction and FoS simulated assuming that the vegetation be replaced by a WEC at some point in time.

6.1 Morphological and hydrological characteristics of the 2005 Nocera Inferiore landslide

The landslide area is in the district of Nocera Inferiore in Southern Italy, on the eastern border of the Lattari Mountains and approximately 15 km northwest of Salerno. This region is characterised by pyroclastic SILT slopes of varying thickness and inclinations, primarily formed by the volcanic activity of the Somma-Vesuvius complex. These SILT covers overlay fractured calcareous bedrocks and are susceptible to generating rainfall-induced debris avalanches.

The stratigraphy on gentle slopes includes, from bedrock to ground surface, a basal paleosol of silty sand/sandy silt approximately 1-meter thickness, a layer of pumices (coarse sand and gravel) with a low degree of weathering up to 1 m thickness, and a weathered and pedogenised volcanic ash layer up to 1 m thickness, composed of silty sands/sandy silt (de Vita et al., 2006; de Vita et al., 2018). Steeper slopes exceeding 30° inclination are more susceptible to rainfall-induced landslides. In these areas, the thickness of the pumice layer tends to reduce and disappear when slopes reach around 40° inclination. When the pumice layer tends to disappear, the slope becomes almost homogeneous in terms of hydraulic properties despite being formed by silt layers of different geological origin. This geotechnical homogeneity is observed in the landslide area of the Nocera Inferiore, particularly in the apical zone where the landslide is supposed to have been triggered (Revellino et al., 2013). Similar homogeneity has also been noted in other areas of the Lattari Mountains affected by debris avalanches (Calcaterra et al., 2004, Fiorillo et al., 2004, Forte et al., 2019), such as San Pantaleone Hill (events in 1961, 1972, and 1997) and Monte Pendolo (event in 1971) (Rianna et al., 2023).

The finest fraciton of ash soils (silt with moderate clay fraction) for these SILT slopes is generally non-plastic due to its volcanic origin. Soil porosity can reach up to 70%, with peaks attaining 80%. Over the past 60 years, debris avalanches have involved SILT slopes approximately 2 m thickness, typically triggered by antecedent cumulative rainfall exceeding 500 mm within the same hydrological year and a critical rainfall event characterised by its exceptional duration (up to 15 hours), rather than its intensity. Rianna et al. (2014b) provided a physical interpretation of the rainfall patterns inducing slope instability in these soil covers.

The Nocera Inferiore landslide is the most recent and significant event in the area recorded over the past fifty years and occurred on 4 March 2005. A nearby weather station provided data about the meteorological conditions triggering the landslide, including hourly precipitation, air relative humidity, and air temperature. An antecedent amount of 800 mm characterised the rainfall history since September 1, 2004, and the critical event consisted of 143 mm rainfall over 16 h duration. These conditions are consistent with other rainfall events that have triggered debris avalanches in the Lattari Mountains (Pagano et al., 2010).

After the landslide, a triangular-shaped area was visible (Figure 16). It extended over an open slope with an average inclination of 36° and mobilised a soil mass of 33,000 m^3. The kinematics was typical of a debris avalanche. The SILT slope angle in the apical zone of ~40° slightly exceeded the soil friction angle of 37-39° (Pagano et al., 2010), likely triggering the landslide. The bedrock consisted of highly fractured limestone at 1 to 2 m depth, with the greatest depths in the apical zone. Figure 17 shows the evolution of meteorological forcings in terms of rainfall and reference evaporation over the ten years preceding and following the landslide event (from February 1998 to October 2008).

Coppola, L., Reder, A., Rianna, G., Tarantino, A., & Pagano, L. (in press). Effects of Wooden Embers Cover on thermo-hydrological response of silty volcanic cover and implications to post-wildfire slope stability. *Engineering Geology*.

Figure 16. The 2005 Nocera Inferiore landslide.

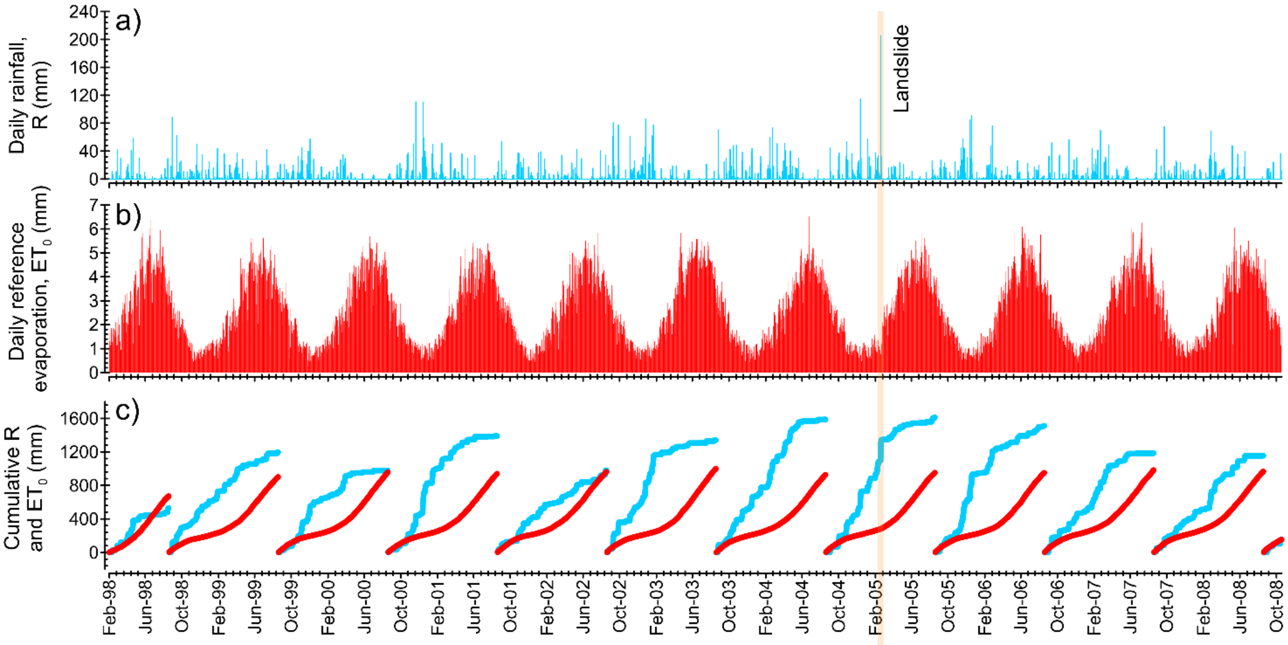

Figure 17. Evolution of meteorological forcing at the landslide site between 1998 and 2008 (landslide event occurred on 4 March 2005). (a) Daily rainfall; (b) Daily reference evapotranspiration; (c) Cumulative rainfall and reference evapotranspiration over a hydrological year

6.2 Simulation of the effect of WEC formation following wildfire on rainfall-induced slope instability

Different mechanisms may contribute to initiate the rainfall-induced instability of the pyroclastic SILT slopes in this area (Coppola et al., 2020). These include i) the reduction of soil shear strength due to loss of suction, ii) the reduction of pullout resistance of roots anchored to the fractured bedrock favoured by loss of suction, and iii) the static liquefaction generated by volumetric collapse occurring when suction reduces and saturation is approached (Olivares, 2001; Olivares & Picarelli, 2003). Regardless of the mechanism, slope failure is driven by the loss of suction generated by infiltrating rainwater. Therefore, the replacement of vegetation with a WEC following a wildfire is expected to affect landslide initiation due to the WEC's effect on the slope's suction regime. An in-depth analysis of the failure of the Nocera Inferiore landslide is out of the scope of this work, and for the sake of simplicity, the attention is only focused here on the first mechanism, i.e., the reduction of soil shear strength due to the loss of suction.

Pagano et al. (2019) simulated the effect of the 10-year meteorological time series (Figure 17) on the suction regime in the Nocera Inferiore SILT slope. The coupled thermohydraulic analysis was performed under 1D conditions considering a column 2 m high and the constitutive thermohydraulic model for the SILT presented in Section 3. Meteorological data were converted into evapotranspiration boundary flux according to the approach by Tratch et al. (1995). The evapotranspiration was split into an evaporation and a transpiration component. Transpiration-induced flux was distributed along the root zone mesh nodes, and the flux imposed at each node was ‘reduced’ using the Feddes reduction function (Feddes et al., 1998). Evaporation-induced flux was applied at the surface, and the actual evaporation was modelled by considering Wilson’s reduction function (Eq. [12]).

Figure 18a shows the suction simulated for the vegetated slope at the depth of 1.5 m (taken as representative of the average depth of the failure surface) starting from June 2000. The Factor of Safety (FoS) of the slope was computed by considering the case of infinite slope and a failure surface located at the depth *z*=1.5m:

$$FoS = \frac{\tan\varphi'}{tan\beta} + \frac{s\ \ S_r \tan\varphi'}{\gamma\ z\ \sin\beta\cos\beta} \qquad [13]$$

where γ is soil unit weight (10.6 kN/m^3), φ'= friction angle (φ'= 37°), S_r is the degree of saturation, *s* is the suction, *z* is the depth of the potential failure surface (*z*=1m), and β is the inclination of the slope. As shown in Figure 18b, the FoS follows the fluctuation of suction and reaches minima during the winter periods. The FoS reduced to values lower than unity when the landslide occurred in March 2005.

a)

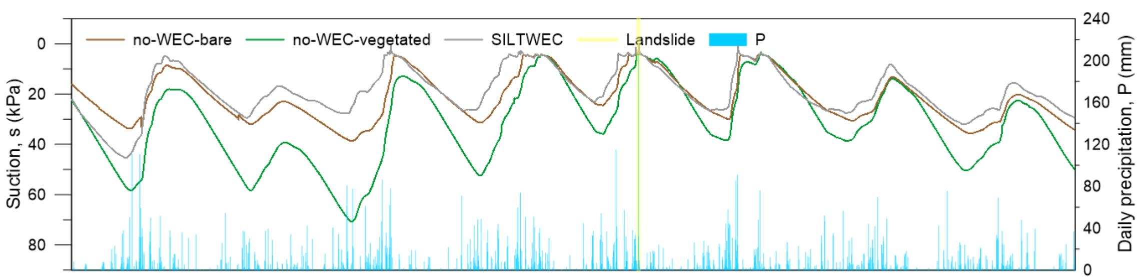

Coppola, L., Reder, A., Rianna, G., Tarantino, A., & Pagano, L. (in press). Effects of Wooden Embers Cover on thermo-hydrological response of silty volcanic cover and implications to post-wildfire slope stability. *Engineering Geology*.

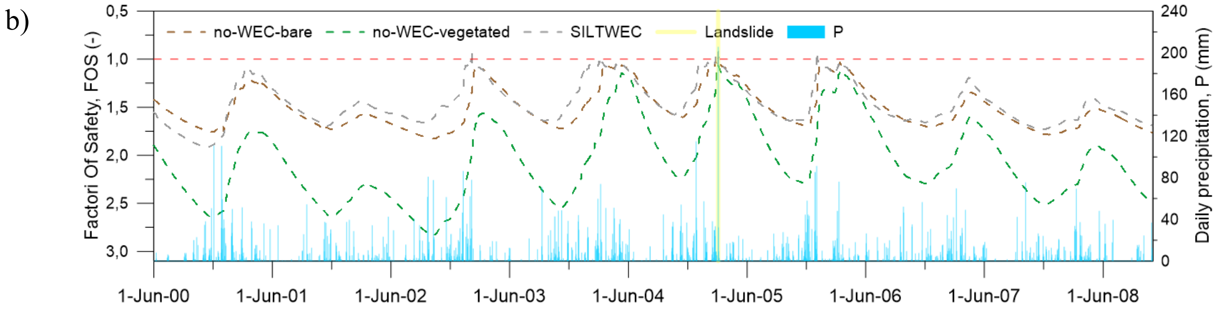

Figure 18. Evolution of suction and Factor of Safety (FoS) at slope mid-depth for the case of vegetated slope (no-WEC-vegetated, green, curve,) and the scenario of WEC replacing the vegetation following wildfire on 1 June 2000 (SILTWEC,grey, curve). The case of bare soil (vegetation removed without the formation of a WEC) is also shown for comparison (no-WEC-bare, brown curve). (a) Suction; (b) FoS.

A wildfire was assumed to occur on 1 June 2000, simulating WEC formation effects by i) removing the evapotranspiration boundary flux, ii) adding a 5 cm thick WEC on the top of the SILT layer, and iii) applying an evaporation boundary flux at the top of the WEC. Figure 18b shows that, in the case of wildfire and WEC formation, failure would have occurred two years earlier (in Winter 2003).

A wildfire is responsible for the loss of root water uptake mechanism and the formation of a WEC thermohydraulic barrier. To discriminate between these two effects, the case of bare soil was also simulated (no-WEC-bare condition) by replacing the evapotranspiration with the evaporation boundary flux without adding WEC layer on the top of the SILT slope. The bare soil maintains the same evaporative flux as the vegetated cover. Still, it does not distribute the water uptake over the root zone and does not generate the thermohydraulic barrier effect as the WEC. Figure 18b shows that the no-WEC-bare curve lies between the no-WEC-vegetated and SILTWEC curves, indicating that both the deactivation of transpiration effects and the WEC formation reduce FoS significantly following a wildfire.

7. Conclusions

The paper has presented a multi-year experimental investigation into the effect of Wooden Embers Cover (WEC) overlying a layer of pyroclastic silt (SILT) on the hydrological regime of the SILT layer. The WEC simulates the formation of a cover following wildfire. This experiment aimed to explore whether the thermo-hydraulic properties of the WEC have beneficial or adverse effect on rainfall-induced instability of pyroclastic SILT slopes. Experiments were conducted in an outdoor lysimeter filled with SILT up to 75 cm covered with 5cm of WEC. Water storage in the SILT layer, soil water content, suction, and temperature were recorded for 3 years (SILT+WEC condition, 2019-2022) and compared with the hydrological regime recorded in antecedent experiments in the same lysimeter including bare condition (4 years, 2010-2014) and vegetated condition (5 years, 2014-2019).

The WEC reduces water losses by evaporation thus increasing the average water content in the underlying SILT, an effect that is detrimental to slope stability. The barrier effect can be in principle associated with the lower thermal conductivity of the WEC, which was reflected by the lower soil temperatures recorded when the WEC was in place. The lower is the energy supplied to the underlying SILT layer, the lower is the energy made available for the phase transition from liquid to vapour water, in turn reducing the 'internal' evaporation. A second effect can be associated with the lower hydraulic conductivity of the WEC layer at high suctions, which develop in the WEC over dry periods.

To discriminate between these two effects, a numerical simulation was carried out by comparing the case of a WEC with its real thermal and hydraulic properties with the case of a fictitious top layer placed on the top of the SILT having the same hydraulic properties of the WEC but the thermal properties of the SILT. Negligible differences were observed between the simulated suction at different depths leading to the conclusion that the barrier effect of the WEC is mainly associated with its hydraulic properties, i.e. the WEC acts as a capillary barrier.

The lysimeter data show that replacing the vegetation with a WEC generated an increase in water storage of around 200 mm at the end of the dry season, with the SILT having reduced potential to store rainwater during the subsequent wet season making it more susceptible to rainfall-induced instability. Landslides in pyroclastic soil are associated with antecedent rainfall of 500-700 mm and a triggering high-intensity rainfall events that release 80-150 mm of rains over tens of hours; these numbers indicate that 200 mm of reduced water storage could be fatal for the slope during a wet period after a wildfire.

To gain a quantitative insight into the effect of a WEC on the susceptibility of SILT slopes to rainfall-induced landsliding, the case study of the 2005 Nocera Inferiore landslide was reanalysed by simulating the presence of a WEC following a wildfire. The numerical analyses show that the WEC makes the SILT slope vulnerable to less severe rainfall events. For the scenario considered, the landslide would have occurred two years earlier.

Achronimous	Description
SILT	layer of silty volcanic soil
WEC	wooden embrace cover
no-WEC-bare	SILT without WEC and bare conditions
no-WEC-vegetated	SILT without WEC and presence of a grass
SILT WEC	layer of silty volcanic soil with superimposed a wooden embrace cover, each material has its own thermal and hydraulic properties
SILT WECh	layer of silty volcanic soil with superimposed a wooden embrace cover, WEC layer has the thermal properties of the SILT
SILT80	WEC layer replaced with SILT layer

List of notations

Symbol	Unit	Description

θ	[-]	volumetric water content
θ_s	[-]	volumetric water content at saturation
θ_r	[-]	volumetric water content at residual state
θ_e	[-]	effective degree of saturation
α	[1/kPa]	water retention function parameter
n	[-]	water retention function parameter
m	[-]	water retention function parameter
k_{sat}	[m/s]	saturated hydraulic conductivity
λ	[W/mK]	thermal conductivity
c_v	[J/m^{3}K]	volumetric specific heat
q_t	[W/m]	heat per unit length supplied to heat dissipation probe
ΔT	[K]	temperature change
Δt	[s]	time span
φ_s	[-]	volumetric fraction of solid matrix
c_s	[MJ/m^{3}K]	volumetric specific heat of solid
ρ_s	[g/cm^3]	density of solid matrix
φ_w	[-]	volumetric fraction of water
c_w	[MJ/m^{3}K]	volumetric specific heat of water
ρ_w	[g/cm^3]	density of water
ch_0	[J/m^{3}K]	volumetric specific heat function parameter
a_0	[J/m^{3}K]	volumetric specific heat function parameter
b_0	[-]	volumetric specific heat function parameter
u_w	[kPa]	liquid pore-water pressure
u_a	[kPa]	pore air pressure
u_v	[kPa]	partial pressure of vapour pore-water
m_2^w	[1/kPa]	slope of soil water retention curve
P_a	[kPa]	total atmospheric pressure
k_w	[m/s]	hydraulic conductivity function
D_v	[°C]	vapour diffusivity through the soil
g	[m/s^2]	gravitational acceleration
L_v	[J/kg]	latent heat of water vaporisation
u_{v0}	[kPa]	saturated partial pressure of pore vapour
M_w	[kg/mol]	water molecular weight
R	[J/mol°C]	ideal gas constant
AE	[kg/m^{2}s]	actual evaporation

Coppola, L., Reder, A., Rianna, G., Tarantino, A., & Pagano, L. (in press). Effects of Wooden Embers Cover on thermo-hydrological response of silty volcanic cover and implications to post-wildfire slope stability. *Engineering Geology*.

k	[-]	reduction function
PE	[kg/m^{2}s]	potential evaporation
RE	[kg/m^{2}s]	potential evaporation rate from a reference surface
k_{crop}	[-]	crop coefficient
T_a	[°C]	air temperature
u_{2m}	[m/s]	wind speed at 2 m above the surface of the ground
Δ	[Pa/°C]	slope of the saturation vapour pressure curve at the air temperature t_a
γ	[Pa/°C]	psychrometric constant at the air temperature t_a
Rn	[W/m^2]	net radiation
G	[W/m^2]	soil heat flux
φ'	[°]	friction angle
γ	[kN/m^3]	soil unit weight
S_r	[-]	degree of saturation
β	[°]	inclination of the slope

8. References

Abdollahi, M., Vahedifard, F., & Leshchinsky, B. A. (2024). Hydromechanical modeling of evolving post-wildfire regional-scale landslide susceptibility. *Engineering Geology*, *335*, 107538.

Al Qadad, A., Shahrour, I., & Rouainia, M. (2012). Influence of the soil-atmosphere exchange on the hydric profile induced in soil-structure system. *Natural Hazards and Earth System Sciences*, *12*(6), 2039-2049. https://doi.org/10.5194/nhess-12-2039-2012

Allen, R. G., Pereira, L. S., Raes, D., & Smith, M. (1998). FAO Irrigation and drainage paper No. 56. Rome: *Food and Agriculture Organization of the United Nations*, 56(97), e156.

Bernard, D., Trousil, E., & Santi, P. (2021). Estimation of inundation areas of post-wildfire debris flows in Southern California USA. *Engineering Geology*, *285*, 105991.

Bordoloi, S., & Ng, C. W. W. (2020). The effects of vegetation traits and their stability functions in bio-engineered slopes: A perspective review. *Engineering Geology*, *275*, 105742.

Calcaterra, D., & Santo, A. (2004). The January 10, 1997 Pozzano landslide, Sorrento Peninsula, Italy. *Engineering Geology*, *75*(2), 181-200.

Cerdà, A. (1998). Changes in overland flow and infiltration after a rangeland fire in a Mediterranean scrubland. *Hydrological processes*, *12*(7), 1031-1042. https://doi.org/10.1002/(SICI)1099-1085(19980615)12:7<1031::AID-HYP636>3.0.CO;2-V

Coppola, L., Reder, A., Rianna, G., Tarantino, A., & Pagano, L. (in press). Effects of Wooden Embers Cover on thermo-hydrological response of silty volcanic cover and implications to post-wildfire slope stability. *Engineering Geology*.

Cerdà, A., & Doerr, S. H. (2008). The effect of ash and needle cover on surface runoff and erosion in the immediate post-fire period. *Catena*, *74*(3), 256-263. https://doi.org/10.1016/j.catena.2008.03.010

Coppola, L., Reder, A., Rianna, G., & Pagano, L. (2020). The role of cover thickness in the rainfall-induced landslides of Nocera Inferiore 2005. *Geosciences*, 10(6), 228. doi:10.3390/geosciences10060228

Cui, Y., & Shao, J. (2005). The role of ground water in arid/semiarid ecosystems, Northwest China. *Groundwater*, *43*(4), 471-477. https://doi.org/10.1111/j.1745-6584.2005.0063.x

De Vita, P.; Celico, P.; Siniscalchi, M.; Panza, R. (2006). Distribution, hydrogeological features and landslide hazard of pyroclastic soils on carbonate slopes in the area surrounding Mount Somma-Vesuvius. *Italian J. Eng. Geol. Environ*. 1, 1–24.

De Vita, P.; Fusco, F.; Tufano, R.; Cusano, D. (2018). Seasonal and Event-Based Hydrological and Slope Stability Modeling of Pyroclastic Fall Deposits Covering Slopes in Campania (Southern Italy). *Water*, 10, 1140, doi:10.3390/w10091140.

De Vries, D. A. (1963). Thermal properties of soils. *Physics of plant environment.*, 210-235.

Ebel, B. A., Moody, J. A., & Martin, D. A. (2012). Hydrologic conditions controlling runoff generation immediately after wildfire. *Water Resources Research*, *48*(3). https://doi.org/10.1029/2011WR011470

Esposito, G., Gariano, S. L., Masi, R., Alfano, S., & Giannatiempo, G. (2023). Rainfall conditions leading to runoff-initiated post-fire debris flows in Campania, Southern Italy. *Geomorphology*, *423*, 108557. https://doi.org/10.1016/j.geomorph.2022.108557

Feddes, R.A., Kowaklik, P.J., and Zaradny, H. 1978. Simulation of field water use and crop yield. John Wiley and Sons.

Ferreira, A. J., Silva, J. S., Coelho, C., Boulet, A. K., & Keizer, J. J. (2009). The Portuguese experience in managing fire effects. In *Fire effects on soils and restoration strategies* (pp. 417-438). CRC Press.

Filis, C., Spyrou, N. I., Diakakis, M., Kotroni, V., Lagouvardos, K., Papagiannaki, K., Vassilakis, E., Milios, D., and Lekkas, E.: Post-wildfire flash flooding in small mountainous catchments: post-fire effects and characteristics of the November 2019 flash flood in Kineta, Greece, EGU General Assembly 2020, Online, 4–8 May 2020, EGU2020-5501, https://doi.org/10.5194/egusphere-egu2020-5501, 2020.

Fiorillo, F., & Wilson, R. C. (2004). Rainfall induced debris flows in pyroclastic deposits, Campania (southern Italy). *Engineering Geology*, *75*(3-4), 263-289.

Forte, G., Pirone, M., Santo, A., Nicotera, M. V., & Urciuoli, G. (2019). Triggering and predisposing factors for flow-like landslides in pyroclastic soils: the case study of the Lattari Mts.(southern Italy). *Engineering Geology*, *257*, 105137.

Coppola, L., Reder, A., Rianna, G., Tarantino, A., & Pagano, L. (in press). Effects of Wooden Embers Cover on thermo-hydrological response of silty volcanic cover and implications to post-wildfire slope stability. *Engineering Geology*.

Gehring, E., Conedera, M., Maringer, J. *et al.* (2019) Shallow landslide disposition in burnt European beech (*Fagus sylvatica* L.) forests. *Sci Rep* 9, 8638. https://doi.org/10.1038/s41598-019-45073-7

Gerrits, A. M. J. (2010). The role of interception in the hydrological cycle. (Doctoral dissertation, Delft University of Technology)

Gitirana Jr, G. (2005). *Weather-related geo-hazard assessment model for railway embankment stability* (Doctoral dissertation, University of Saskatchewan).

Hillel, D. (2013) Introduction to Soil Physics. Academic Press Limited, Oval Road, London, 1982, pp. 24-28.

Kampf, S. K., Brogan, D. J., Schmeer, S., MacDonald, L. H., & Nelson, P. A. (2016). How do geomorphic effects of rainfall vary with storm type and spatial scale in a post-fire landscape?. *Geomorphology*, *273*, 39-51. https://doi.org/10.1016/j.geomorph.2016.08.001

Kean, J. W., Staley, D. M., & Cannon, S. H. (2011). In situ measurements of post-fire debris flows in southern California: Comparisons of the timing and magnitude of 24 debris-flow events with rainfall and soil moisture conditions. *Journal of Geophysical Research: Earth urface*, *116*(F4). https://doi.org/10.1029/2011JF002005

Lainas, S., Depountis, N., & Sabatakakis, N. (2021). Preliminary Forecasting of Rainfall-Induced Shallow Landslides in the Wildfire Burned Areas of Western Greece. *Land*, *10*(8), 877. https://doi.org/10.3390/land10080877

Larsen, I. J., MacDonald, L. H., Brown, E., Rough, D., Welsh, M. J., Pietraszek, J. H., ... & Schaffrath, K. (2009). Causes of post-fire runoff and erosion: Water repellency, cover, or soil sealing?. *Soil Science Society of America Journal*, *73*(4), 1393-1407. https://doi.org/10.2136/sssaj2007.0432

Letey, J. (2001). Causes and consequences of fire-induced soil water repellency. *Hydrological Processes*, *15*(15), 2867-2875. https://doi.org/10.1002/hyp.378

Lourenço, L., Nunes, A. N., Bento-Gonçalves, A., & Vieira, A. (2012). Soil erosion after wildfires in Portugal: What happens when heavy rainfall events occur. *Research on soil erosion*, 65-88. DOI: 10.5772/50447

MacDonald, L. H., & Huffman, E. L. (2004). Post-fire soil water repellency: persistence and soil moisture thresholds. *Soil Science Society of America Journal*, *68*(5), 1729-1734. https://doi.org/10.2136/sssaj2004.1729

Marshall, T.J., Holmes, J.W. & Rose, C.W. (1996) Soil physics, 3rd edn.Cambridge University Press, Cambridge, UK

Coppola, L., Reder, A., Rianna, G., Tarantino, A., & Pagano, L. (in press). Effects of Wooden Embers Cover on thermo-hydrological response of silty volcanic cover and implications to post-wildfire slope stability. *Engineering Geology*.

Mayor, A. G., Bautista, S., Llovet, J., & Bellot, J. (2007). Post-fire hydrological and erosional responses of a Mediterranean landscpe: Seven years of catchment-scale dynamics. *Catena*, *71*(1), 68-75. https://doi.org/10.1016/j.catena.2006.10.006

Melo, R., van Asch, T., & Zêzere, J. L. (2018). Debris flow run-out simulation and analysis using a dynamic model. *Natural Hazards and Earth System Sciences*, *18*(2), 555-570. https://doi.org/10.5194/nhess-18-555-2018, 2018.

Milly, P. C. D. (1982). Moisture and heat transport in hysteretic, inhomogeneous porous media: A matric head-based formulation and a numerical model. *Water Resources Research*, *18*(3), 489-498. https://doi.org/10.1029/WR018i003p00489

Nicotera, M., Papa, R., & Urciuoli, G. (2010). An experimental technique for determining the hydraulic properties of unsaturated pyroclastic soils. *Geotechnical Testing Journal*, *33*(4), 263-285. DOI: 10.1520/GTJ102769

Olivares, L. (2001). Static liquefaction: An hypothesis for explaining transition from slide to flow in pyroclastic soils. In Proceedings of the Transition from Slide to Flow: Mechanisms and Remedial Measures, Trabzon, Turkey, 25–26 August 2001 [CD-ROM]; Karadeniz Technical University, Trabzon, Turkey.

Olivares, L., & Picarelli, L. (2003). Shallow flowslides triggered by intense rainfalls on natural slopes covered by loose unsaturated pyroclastic soils. *Géotechnique*, 53(2), 283-287.

Pagano, L., Picarelli, L., Rianna, G., & Urciuoli, G. (2010). A simple numerical procedure for timely prediction of precipitation-induced landslides in unsaturated pyroclastic soils. *Landslides*, 7, 273-289. DOI 10.1007/s10346-010-0216-x

Pagano, L., Reder, A., & Rianna, G. (2019). Effects of vegetation on hydrological response of silty volcanic covers. *Canadian Geotechnical Journal*, *56*(9), 1261-1277. https://doi.org/10.1139/cgj-2017-0625

Raymond, C. A., McGuire, L. A., Youberg, A. M., Staley, D. M., & Kean, J. W. (2020). Thresholds for post-wildfire debris flows: Insights from the Pinal Fire, Arizona, USA. *Earth Surface Processes and Landforms*, *45*(6), 1349-1360. https://doi.org/10.1002/esp.4805

Reder, A., Pagano, L., Picarelli, L., & Rianna, G. (2017). The role of the lowermost boundary conditions in the hydrological response of shallow sloping covers. *Landslides,* 14, 861-873. https://doi.org/10.1007/s10346-016-0753-z

Reder, A., Rianna, G., & Pagano, L. (2018). Physically based approaches incorporating evaporation for early warning predictions of rainfall-induced landslides. *Natural Hazards and Earth System Sciences*, *18*(2), 613-631. https://doi.org/10.5194/nhess-18-613-2018

Coppola, L., Reder, A., Rianna, G., Tarantino, A., & Pagano, L. (in press). Effects of Wooden Embers Cover on thermo-hydrological response of silty volcanic cover and implications to post-wildfire slope stability. *Engineering Geology*.

Rengers, F. K., McGuire, L. A., Oakley, N. S., Kean, J. W., Staley, D. M., & Tang, H. (2020). Landslides after wildfire: Initiation, magnitude, and mobility. *Landslides*, *17*, 2631-2641. https://doi.org/10.1007/s10346-020-01506-3

Revellino, P.; Guerriero, L.; Gerardo, G.; Hungr, O.; Fiorillo, F.; Esposito, L.; Guadagno, F.M. (2013). Initiation and propagation of the 2005 debris avalanche at Nocera inferior (Southern Italy*). Italian J. Geosci*., 132, 366–379, doi:10.3301/IJG.2013.02.

Rianna, G., Pagano, L., & Urciuoli, G. (2012). A physical model to investigate the influence of atmospheric variables on soil suction in pyroclastic soils. In *Unsaturated Soils: Research and Applications: Volume 2* (pp. 221-227). Springer Berlin Heidelberg. https://doi.org/10.1007/978-3-642-31343-1_28

Rianna, G., Pagano, L., & Urciuoli, G. (2014a). Rainfall patterns triggering shallow flowslides in pyroclastic soils. *Engineering Geology*, *174*, 22-35. https://doi.org/10.1016/j.enggeo.2014.03.004

Rianna, G., Pagano, L., & Urciuoli, G. (2014b). Investigation of soil–atmosphere interaction in pyroclastic soils. *Journal of hydrology*, *510*, 480-492. https://doi.org/10.1016/j.jhydrol.2013.12.042

Rianna, G., Reder, A., & Pagano, L. (2023). From empirically to physically based early warning predictions of rainfall-induced landslides in silty volcanic soils: the Lattari Mountains case study. *Bulletin of Engineering Geology and the Environment*, 82(6), 223.

Shakesby, R. A., & Doerr, S. H. (2006). Wildfire as a hydrological and geomorphological agent. *Earth-Science Reviews*, *74*(3-4), 269-307. https://doi.org/10.1016/j.earscirev.2005.10.006

Shiozawa, S., & Campbell, G. S. (1990). Soil thermal conductivity. *Remote Sensing Reviews*, *5*(1), 301-310.https://doi.org/10.1080/02757259009532137

Silva, J.S., Rego, F., Fernandes, P., Rigolot, E., 2010. Towards Integrated Fire Management e Outcomes of the European project fire Paradox. In: *European Forest Institute Research Report*, vol. 23, 241 pp

Staley, D. M., Kean, J. W., & Rengers, F. K. (2020). The recurrence interval of post-fire debris-flow generating rainfall in the southwestern United States. *Geomorphology*, *370*, 107392. https://doi.org/10.1016/j.geomorph.2020.107392

Staley, D. M., Kean, J. W., Cannon, S. H., Schmidt, K. M., & Laber, J. L. (2013). Objective definition of rainfall intensity–duration thresholds for the initiation of post-fire debris flows in southern California. *Landslides*, *10*, 547-562. https://doi.org/10.1007/s10346-012-0341-9

Tetens O. 1930. Uber einige meteorologische.Begriffe, Zeitchrift fur Geophysik6: 297–309.

Tratch, D.J., Wilson, G.W., and Fredlund, D.G. 1995. An introduction to analytical modeling of plant transpiration for geotechnical engineers. *In* Proceedings of the 48th Canadian Geotechnical Conference, Vancouver, B.C., 25–27 September 1995. Vol. 2, pp. 771–780.

Coppola, L., Reder, A., Rianna, G., Tarantino, A., & Pagano, L. (in press). Effects of Wooden Embers Cover on thermo-hydrological response of silty volcanic cover and implications to post-wildfire slope stability. *Engineering Geology*.

Van Genuchten, M. T. (1980). A closed-form equation for predicting the hydraulic conductivity of unsaturated soils. *Soil science society of America journal*, *44*(5), 892-898.

Vergani, C., Werlen, M., Conedera, M., Cohen, D., & Schwarz, M. (2017). Investigation of root reinforcement decay after a forest fire in a Scots pine (Pinus sylvestris) protection forest. *Forest Ecology and Management*, *400*, 339-352. https://doi.org/10.1016/j.foreco.2017.06.005

Waples, D. W., & Waples, J. S. (2004). A review and evaluation of specific heat capacities of rocks, minerals, and subsurface fluids. Part 1: Minerals and nonporous rocks. *Natural resources research*, *13*, 97-122. https://doi.org/10.1023/B:NARR.0000032647.41046.e7

Wilson, G. W., Fredlund, D. G., & Barbour, S. L. (1994). Coupled soil-atmosphere modelling for soil evaporation. *Canadian geotechnical journal*, *31*(2), 151-161. https://doi.org/10.1139/t94-021

Wilson, G. W., Fredlund, D. G., & Barbour, S. L. (1997). The effect of soil suction on evaporative fluxes from soil surfaces. *Canadian Geotechnical Journal*, *34*(1), 145-155. https://doi.org/10.1139/t96-078

Yuan-jun, J., Alam, M., Li-Jun, S., Umar, M., Sadiq, S., Jia, L. J., & Rahman, M. (2022). Effect of root orientation on the strength characteristics of loess in drained and undrained triaxial tests. *Engineering Geology*, *296*, 106459.